Journal of the Mechanics and Physics of Solids 88 (2016) 291–319

Contents lists available at ScienceDirect

Journal of the Mechanics and Physics of Solids

journal homepage: www.elsevier.com/locate/jmps

Homogenization of viscoplastic constitutive laws within a phase field approach

Victor de Rancourt [a], Kais Ammar [a], Benoît Appolaire [b,*], Samuel Forest [a]

[a] Mines ParisTech, Centre des Matériaux / CNRS UMR 7633, BP 87, 91003 Evry cedex, France
[b] LEM, CNRS/ONERA UMR 104, 29 Av. Division Leclerc, BP 72, 92322 Châtillon, France

ARTICLE INFO

Article history:
Received 20 May 2015
Received in revised form
29 October 2015
Accepted 30 December 2015
Available online 7 January 2016

Keywords:
Phase field
Homogenization
Viscoplasticity
Crystal plasticity
Phase transformation
Diffusion

ABSTRACT

The present work provides an original consistent framework for combining different constitutive laws, possibly nonlinear, within diffuse interface models (phase field) by homogenization rather than by mixing the material parameters, such as to offer a greater flexibility. The framework relies on the choice of relevant thermodynamic potentials such that the homogenization schemes are natural choices in the thermodynamic formulation. Thus, it justifies previously proposed classic schemes (Ammar et al., 2009b) and gives clues to explore new schemes (Durga et al., 2013; Mosler et al., 2014) by defining relevant potentials. The proposed framework is illustrated by addressing two issues. First, Reuss and Voigt homogenization schemes are shown to deliver the same kinetics of diffusion-controlled transformations in the pure elastic case in the limit of vanishing diffuse interface width. Second, using the Voigt homogenization scheme, we demonstrate that the influence of viscoplasticity, either isotropic or crystalline, on diffusion-controlled transformations is non-trivial and cannot be inferred from simple qualitative arguments. Depending on the competition between the time scales of diffusion and viscoplasticity, the growth kinetics may exhibit intermediate behaviors between purely chemical and elastic cases. Moreover, it is shown how viscoplasticity can change the morphological stability of growing circular precipitates.

© 2015 Elsevier Ltd. All rights reserved.

1. Introduction

The phase field approach has become a ubiquitous tool to simulate microstructure evolutions in materials undergoing phase transformations (Steinbach, 2009; Finel et al., 2010). Phases are described by continuous fields where each one is endowed with a transport equation, or phase field equation. Such fields vary rapidly inside the phase boundaries over a given width, which is also called the interface thickness. The interface is then said to be diffuse, which can have a physical justification when the thickness comes close to a few inter-atomic distances. The transport equations associated to the phase field variables allow us to predict the evolving morphology of new phases, and naturally embed the phase transformation kinetics. For many diffusion-controlled phase transformations, stresses can play a significant role in both the transformation kinetics and the morphology evolution of the growing phases. The transport equations for phase fields were firstly coupled to Cauchy's first law of motion restricted to the elastic behavior of the phases in Wang et al. (1993) and Dreyer and Müller

* Corresponding author.
E-mail addresses: victor.de_rancourt@mines-paristech.fr (V. de Rancourt), kais.ammar@mines-paristech.fr (K. Ammar), benoit.appolaire@onera.fr (B. Appolaire), samuel.forest@mines-paristech.fr (S. Forest).

http://dx.doi.org/10.1016/j.jmps.2015.12.026
0022-5096/© 2015 Elsevier Ltd. All rights reserved.

(2000). More recently, the attention was focused on the extension to plasticity and viscoplasticity, as done by Guo et al. (2005), Ubachs et al. (2005), Uehara et al. (2007), Gaubert et al. (2008, 2010), Yamanaka et al. (2008), Ammar et al. (2009b), and Schmitt et al. (2014).

Two main approaches have been proposed to determine the effective behavior of the interface. They are namely the interpolation and homogenization approaches according to the terminology by Ammar et al. (2009b, 2011, 2014). These methods are closely related to the "coarse-graining" and the "two-phase" approaches mentioned in Plapp (2011), respectively. In the latter reference, and in the "two-phase" approach, the diffuse interface is "*seen as a mixture of two phases that each retain their macroscopic properties*", and for which standard homogenization methods coming for instance from the mechanics of heterogeneous materials (Sanchez-Palencia and Zaoui, 1987; Zaoui, 2002; Qu and Cherkaoui, 2006; François et al., 2012), can be used to derive the effective response. In this case, the phase field parameter then plays a role akin to the volume fraction of one phase within the diffuse interface. In contrast, a single constitutive behavior is used for both phases in the interpolation approach for which the corresponding material parameters are interpolated between the bounding values reached in each phase.

The choice of an homogenization relation for the interface effective behavior originates from the work of Tiaden et al. (1998) who introduced two concentration fields on the basis of the mixture theory. Kim et al. (1999) have then recognized that such a solute partitioning, combined with a Reuss like assumption called quasi-equilibrium condition, could remove a spurious contribution to the interfacial energy scaling with the interface thickness. Later on, by analogy to the work of Kim et al. (1999) and Steinbach and Apel (2006) have used the Reuss assumption to describe the elastic behavior within diffuse interfaces. Ammar et al. (2009b, 2011, 2014) also applied the Voigt homogenization scheme that relies on identical strain values taken by both phases at each material point. Very recently, mixed schemes as they arise in laminate microstructures have been proposed by Durga et al. (2013) and Mosler et al. (2014) in order to reduce spurious stress concentration within the interface. Nevertheless, the popularity of the interpolation method, known as Katchaturyan's approach, was such that the first attempts to introduce nonlinear material behavior of phases relied on the interpolation method, see for instance Guo et al. (2005), Gaubert et al. (2008, 2010) and Cottura et al. (2012).

The choice of a suitable homogenization scheme generally depends on the morphology of the mixture of phases within the diffuse interface. As such a mixture very often does not correspond to a physical reality of actual interfaces. This is why various schemes have been applied without reference to the real structure of the interface. But the homogenization and interpolation schemes can be of practical importance with respect to the convergence of the diffuse interface problem on the sharp interface problem. It is now admitted that the Reuss-like assumption done in Kim et al. (1999) improves such a convergence. Finally, Ammar et al. (2014) highlighted the paradigm of the interpolation and homogenization method though the concept of inheritance. The interpolation method embeds inheritance of the internal variables during the phase transformation. On the contrary, the homogenization method makes the internal variables of each phase independent from each other. Nevertheless, inheritance can be added or discarded by the use of suitable evolutionary laws for the internal variables.

Although there have been significant recent advances along this line, in particular in Durga et al. (2013) and in Mosler et al. (2014) for purely elastic and elasto-plastic behaviors respectively, the present study addresses two novel aspects that have not been dealt with so far:

(i) we settle the thermodynamic foundations for the formulation of homogenization based phase field models;
(ii) we perform a systematic computational analysis of the response of the proposed models in the presence of crystal viscoplasticity.

Hence, we first present in Sections 2–4 the constitutive setting based on an original thermodynamic framework extending the continuum thermodynamic framework used in nonlinear mechanics of materials to the phase field approach (Germain et al., 1983; Maugin, 1992, 1999). Second, based on the implementation of Ammar et al. (2009a), this framework is applied in Section 5 to investigate the diffusion controlled growth of precipitates associated with eigenstrains responsible for the activation of plasticity during transformation. Finally, the major achievements are summarized in the conclusion together with a few remaining issues to address.

2. Phase field modeling within the homogenization approach

In the present work, the role of thermodynamics is emphasized, and especially the second law or entropy principle, in selecting suitable homogenization schemes in the phase field models. The constitutive setting is presented based on an original thermodynamic framework extending the continuum thermodynamic framework used in nonlinear mechanics of materials to the phase field approach (Germain et al., 1983; Maugin, 1992, 1999). It heavily relies on the exploitation of the second principle of thermodynamics in order to formulate constitutive assumptions systematically ensuring the positivity of the dissipation rate at each time and at each material point. This represents an alternative to the use of variational derivatives of the free energy function as done classically in phase field approaches since the pioneering work by Cahn and Hilliard (1958). It has the advantage that the theory can be readily applied to finite bodies with specific and unambiguous boundary conditions, in contrast to usual periodic or infinite microstructures and corresponding vanishing boundary

conditions used in the latter reference. The space of state variables is extended to include internal variables accounting for material work-hardening. Mechanical dissipation then results from the competition between energy storage due to the multiplication of dislocations and to dissipation induced by dislocation motion. The theory is suitable for the material evolution at a mesoscale where individual dislocations are not resolved but rather represented by suitable densities. It typically applies at the grain scale in a polycrystal where the continuum crystal plasticity has proved in many cases to provide a reliable description of slip processes. The introduction of crystal plasticity into phase field models goes back to works by Gaubert et al. (2008, 2010) and Cottura et al. (2012) for single crystals and by Abrivard et al. (2012a, 2012b) for polycrystals, including grain boundary migration.

The framework also encompasses the consideration of continuum damage mechanics because the additional internal variables can account for material weakening by cavity growth or micro-cracking (Lemaitre and Chaboche, 1994; Lemaitre and Desmorat, 2004; Besson, 2004; Besson et al., 2009). In this field, phase field approaches meet gradient damage mechanical models as recognised recently in the literature (Forest, 2009; Miehe et al., 2010; Aslan and Forest, 2011; Forest et al., 2011, 2014). A common thermodynamic framework exists that reconciles gradient damage and phase field approaches as used in recent works by Hofacker and Miehe (2012, 2013), Borden et al. (2012), Voyiadjis and Mozaffari (2013), Vignollet et al. (2014), and Ambati et al. (2015) for isotropic materials and Aslan and Forest (2009) and Aslan et al. (2011b, 2011a) in combination with crystal plasticity. However, the discussion in the present work is limited to viscoplasticity, leaving open the possibility of applying the proposed framework for damage applications.

2.1. Description of a two-phase multicomponent material

The present phase field framework is based on the introduction of a phase field parameter ϕ accounting for a two-phase system α–β, with constant values $\phi = 1$ and $\phi = 0$, respectively in α and β. The phase field varies rapidly and continuously from 0 to 1 in the diffuse interface zone over a thickness δ as defined in Kim et al. (1999). The physical degrees of freedom attributed to each material point in the continuum are the concentration c_i of a given chemical element i, and the displacement vector $\underline{\boldsymbol{u}}$ with the corresponding strain tensor $\underset{\sim}{\boldsymbol{\varepsilon}}$ defined as the symmetric part of the gradient of the displacement field.

Following the homogenization method, all of the chosen energy potentials along with their respective state variables, fluxes and conjugates are interpolated as follows:

$$\Xi_i = h(\phi)\Xi_i^{\alpha} + \bar{h}(\phi)\Xi_i^{\beta}, \tag{1}$$

where Ξ can be the Helmholtz free energy density f or the Gibbs free energy density g, the concentration c_i of component i with the conjugate diffusion potential μ_i along with mass flux $\underline{\boldsymbol{J}}_i$, or the strain $\underset{\sim}{\boldsymbol{\varepsilon}}$ and stress $\underset{\sim}{\boldsymbol{\sigma}}$. Accordingly, the quantities Ξ^{α} and Ξ^{β}: c_i^{α}, c_i^{β}, $\underset{\sim}{\boldsymbol{\varepsilon}}^{\alpha}$, etc., can be regarded as fictitious or auxiliary variables in the theory according to Kim et al. (1999) and Ammar et al. (2009b). However, their introduction has been shown to be decisive for a better control of the interfacial properties, in particular when the numerical interface becomes thicker than the physical one. It is worth emphasizing once again that real interfaces at the atomic scale are not two-phase media, and that the general mixture rule Eq. (1) must be seen as a convenient way to gain a better control of interfacial properties and behaviors, rather than ensuing from some volume averaging. Following the earlier phase field models for phase transformations, e.g. Wang et al. (1993), it is required that the weighting function h does not change the position of the minima of the relevant thermodynamic potential (see Sections 3 and 4) with respect to ϕ. Hence, $h(\phi)$, which formally plays the role of a phase fraction in conventional homogenization schemes, must fulfill the additional following requirements:

$$h(1) = 1, \quad h(0) = 0, \qquad h'(\phi) = \begin{cases} 0, & \text{if } \phi = 1 \text{ or } \phi = 0, \\ >0, & \text{if } 0 < \phi < 1. \end{cases} \tag{2}$$

The complementing function $\bar{h}$ is defined as $\bar{h}(\phi) = 1 - h(\phi)$. The conditions on the derivative of h exclude the linear function $h(\phi) = \phi$ emerging from volume averaging in classic homogenization theory. A standard choice for h is the following third-order polynomial function:

$$h(\phi) = \phi^2(3 - 2\phi). \tag{3}$$

Finally, the total strain tensor attributed to each phase at each material point is split into three distinct mechanical contributions as follows:

$$\underset{\sim}{\boldsymbol{\varepsilon}}^{\psi} = \underset{\sim}{\boldsymbol{\varepsilon}}_e^{\psi} + \underset{\sim}{\boldsymbol{\varepsilon}}_p^{\psi} + \underset{\sim}{\boldsymbol{\varepsilon}}_{\star}^{\psi}, \tag{4}$$

where ψ stands for either α or β (the same convention will be adopted in the sequel), and where the subscripts e stands for elasticity, p for (visco-)plasticity and $\star$ for a constant and uniform eigenstrain, the latter being assumed, in this work, to be independent of concentration and temperature, for the sake of brevity.

2.2. Balance equations

The total concentrations are subjected to the local balance of mass in the form:

$$\dot{c}_i + \nabla\cdot\underline{\boldsymbol{J}}_i = 0, \tag{5}$$

for each component i, in the absence of source terms. The mass balance equation is associated with Dirichlet or Neumann conditions at the boundary of the body where the concentration or the normal flux $j = \underline{\boldsymbol{J}}\cdot\underline{\boldsymbol{n}}$ are prescribed, $\underline{\boldsymbol{n}}$ denoting the normal surface vector.

The stress tensor fulfils the static balance of momentum equation:

$$\nabla\cdot\underset{\sim}{\boldsymbol{\sigma}} = \underline{\mathbf{0}}, \tag{6}$$

in the absence of body forces for simplicity. The Cauchy balance equation is complemented by displacement or traction vector, $\underline{\boldsymbol{t}} = \underset{\sim}{\boldsymbol{\sigma}}\cdot\underline{\boldsymbol{n}}$, controlled boundary conditions.

The internal energy density enters the local balance of energy equation

$$\dot{e} = \underset{\sim}{\boldsymbol{\sigma}}\colon\dot{\underset{\sim}{\boldsymbol{\varepsilon}}} - \pi\dot{\phi} + \underline{\boldsymbol{\xi}}\cdot\nabla\dot{\phi}, \tag{7}$$

where generalized stresses $\underline{\boldsymbol{\xi}}$ and π are introduced as dual quantities to the change in phase field parameter ϕ and its gradient, following Gurtin (1996) and Ammar et al. (2009a). The first term in the right-hand side is the classical mechanical power of internal forces whereas the second and third terms account for additional internal energy change associated with boundary motion.

The generalized stresses are postulated to fulfil an additional balance equation in the form:

$$\pi + \nabla\cdot\underline{\boldsymbol{\xi}} = 0. \tag{8}$$

The balance of generalized stresses is associated with Dirichlet or Neumann boundary conditions where the phase field parameter or the generalized stress vector, $\underline{\boldsymbol{\xi}}\cdot\underline{\boldsymbol{n}}$, are prescribed at the boundary.

In the spirit of homogenization theory, the partial quantities c_i^{ψ}, $\underset{\sim}{\boldsymbol{\sigma}}^{\psi}$ are *not* subjected to similar balance equations. This is in contrast to mixture theories as discussed by Müller (2001).

The variational formulation of balance equations (6) and (8) constitutes the generalized principle of virtual power

$$\int_V \left(\underset{\sim}{\boldsymbol{\sigma}}\colon\nabla\underline{\boldsymbol{u}}^* + \pi\phi^* - \underline{\boldsymbol{\xi}}\cdot\nabla\phi^*\right) dV = \int_S \left(\underline{\boldsymbol{n}}\cdot\underset{\sim}{\boldsymbol{\sigma}}\cdot\underline{\boldsymbol{u}}^* - \underline{\boldsymbol{\xi}}\cdot\underline{\boldsymbol{n}}\phi^*\right) dS, \tag{9}$$

using the virtual velocity fields $\{\underline{\boldsymbol{u}}^*, \phi^*\}$, as discussed in Ammar et al. (2009a).

The generalized principle of virtual power is complemented by the variational formulation of the balance of mass equation (5):

$$\int_V \left(\dot{c}_i\, c_i^* - \underline{\boldsymbol{J}}_i\cdot\nabla c_i^*\right) dV = \int_S \left(\underline{\boldsymbol{J}}_i\cdot\underline{\boldsymbol{n}}\right) c_i^*\, dS, \tag{10}$$

for the field of virtual concentration rates c_i^*.

The previous variational formulations are directly applicable to the finite element method. The implementation and the discretization of these equations presented previously in Ammar et al. (2009a) are recalled and extended in Appendices A and B.

3. Constitutive framework based on the Helmholtz free energy potential

Thermodynamic principles are inoperative as long as the state and internal variables of the theory are not defined. This is why the setting up of a constitutive theory starts with the proper definition of the state and internal variables. The internal energy, e, and Helmholtz free energy, f, functions differ by one argument, namely the entropy variable, s, entering the internal energy function and the temperature variable, T, arising in the free energy. They are related by the corresponding Legendre transform:

$$f = e - s\,T. \tag{11}$$

These functions are defined per unit volume in the present work.

The approach is exposed in the case of a two-phase multicomponent system made of solid crystalline materials, as defined in the previous section. To render the model more transparent, its presentation is specialized to the case of a single crystal phase β undergoing plastic slip according to crystal plasticity theory, see Asaro and Lubarda (2006) and Besson et al. (2009), coexisting with phase α which exhibits an isotropic elasto-viscoplastic behavior with no hardening. This does not limit our approach to such a configuration, and it is straightforward to adopt any combination of nonlinear constitutive laws, as will be demonstrated in Section 5.

3.1. State and internal variables

The considered space of state and internal variables for the two-phase α–β system is chosen as:

$$\text{STATE} = \{\phi,\ \nabla\phi,\ c_i^{\alpha},\ \underset{\sim}{\varepsilon}_e^{\alpha},\ c_i^{\beta},\ \underset{\sim}{\varepsilon}_e^{\beta},\ \rho_s^{\beta},\ x_s^{\beta}\}, \tag{12}$$

where ϕ is a smooth phase indicator field, c_i^{ψ} are site fractions occupied by the chemical species i, $\underset{\sim}{\varepsilon}_e^{\psi}$ is the elastic strain tensor attributed to each phase at each material point. The internal variables of the model are represented by the hardening variables, ρ_s^{β} and x_s^{β}, where the subscript s indicates the slip system number according to the crystal plasticity model. The variable ρ_s^{β} is akin to a dislocation density measure directly related to the critical resolved shear stress for the activation of slip system s according to Schmid's law, whereas x_s accounts for kinematic hardening needed for cyclic plasticity. Let N denote the total number of slip systems characterizing the single crystalline phase β, typically $N=12$ in f.c.c. crystals. For simplicity, no hardening variable is introduced in the phase α, without restriction to the generality of the constitutive formulation that allows for distinct behavior laws for both phases. Under general anisothermal conditions, the previous set should be complemented by the temperature variable.

The dual set is composed of the thermodynamic forces associated to the state and internal variables following the framework of continuum thermodynamics:

$$\text{FORCES} = \{-\pi,\ \underline{\xi},\ \mu_i^{\alpha},\ \underset{\sim}{\sigma}^{\alpha},\ \mu_i^{\beta},\ \underset{\sim}{\sigma}^{\beta},\ R_s^{\beta},\ X_s^{\beta}\}, \tag{13}$$

where π and $\underline{\xi}$ are the generalized stresses introduced by Gurtin (1996) and Ammar et al. (2009a), μ_i^{ψ} and $\underset{\sim}{\sigma}^{\psi}$ are respectively the diffusion potentials and stress tensors of phase ψ, R_s^{β} is the slip resistance and X_s^{β} the back-stress as described in Busso and Cailletaud (2005) and Besson et al. (2009) for each slip system s in phase β.

3.2. Decomposition of the free energy density function

The volumetric free energy density f of the two-phase material is decomposed at each material point into diffuse interface, chemical and mechanical parts, respectively called f_{ϕ}, f_c, f_{ε}:

$$f = f_{\phi} + \sum_i f_{c_i} + f_{\varepsilon}. \tag{14}$$

The interface contribution of the free energy density is defined by Kim et al. (1999) as:

$$f_{\phi}(\phi,\nabla\phi) = 3\gamma\left(\frac{1}{\lambda}W(\phi) + \lambda\|\nabla\phi\|^2\right), \tag{15}$$

with γ the interface energy, $\lambda = \delta/(2z)$ where δ is the diffuse interface thickness defined between $\phi^- = 0.05$ and $\phi^+ = 0.95$, z a parameter defined as $z = \log(\phi^+/\phi^-)$ and W the double well function defined as:

$$W(\phi) = \phi^2(1-\phi)^2. \tag{16}$$

Bulk free energies are coupled by means of the phase field variable using the same averaging relations as in Section 2 for the state variables, thermodynamic forces and fluxes (1):

$$f_{c_i}(\phi, c_i^{\alpha}, c_i^{\beta}) = h(\phi) f_{c_i}^{\alpha}(c_i^{\alpha}) + \bar{h}(\phi) f_{c_i}^{\beta}(c_i^{\beta}), \tag{17}$$

$$f_{\varepsilon}(\phi, \underset{\sim}{\varepsilon}_e^{\alpha}, \underset{\sim}{\varepsilon}_e^{\beta}, \rho_s^{\beta}, x_s^{\beta}) = h(\phi) f_{\varepsilon}^{\alpha}(\underset{\sim}{\varepsilon}_e^{\alpha}) + \bar{h}(\phi) f_{\varepsilon}^{\beta}(\underset{\sim}{\varepsilon}_e^{\beta}, \rho_s^{\beta}, x_s^{\beta}). \tag{18}$$

Possible dependence of f_{ε} on concentrations can be added in the latter equation but is not considered here for simplicity, without restriction to the proposed general framework. As a result of the coupling with the phase field variable ϕ shown in Eq. (18), the minimization of the free energy may lead to two phases in equilibrium and, thus, to the construction of diagrams corresponding to chemical equilibrium under mechanical stress, as studied extensively in the references (Cahn and Larché, 1984; Johnson, 1987; Frolov and Mishin, 2012).

3.3. State laws relating thermodynamic variables and their associated forces

The local form of the second principle of thermodynamics is written as:

$$\dot{s} \geq \nabla\cdot\underline{\boldsymbol{\Phi}}, \tag{19}$$

where s is the volumetric entropy density and $\underline{\boldsymbol{\Phi}}$ the entropy density flux. The time derivative of (11) in the isothermal case allows us to rewrite (19) into:

$$\dot{e} - \dot{f} \geq T\,\nabla\cdot\underline{\boldsymbol{\Phi}}. \tag{20}$$

The free energy density is a function of the state variables (12). Its time derivative can be expanded according to the chain rule:

$$\dot{f} = \frac{\partial f}{\partial \phi}\dot{\phi} + \frac{\partial f}{\partial \nabla\phi}\cdot\nabla\dot{\phi} + \sum_i \frac{\partial f}{\partial c_i^\alpha}\dot{c}_i^\alpha + \sum_i \frac{\partial f}{\partial c_i^\beta}\dot{c}_i^\beta + \frac{\partial f}{\partial \underset{\sim}{\boldsymbol{\varepsilon}}_e^{\,\alpha}} : \dot{\underset{\sim}{\boldsymbol{\varepsilon}}}_e^{\,\alpha} + \frac{\partial f}{\partial \underset{\sim}{\boldsymbol{\varepsilon}}_e^{\,\beta}} : \dot{\underset{\sim}{\boldsymbol{\varepsilon}}}_e^{\,\beta} + \sum_s \frac{\partial f}{\partial \rho_s^\beta}\dot{\rho}_s^\beta + \sum_s \frac{\partial f}{\partial x_s^\beta}\dot{x}_s^\beta. \tag{21}$$

The entropy flux is related to the mass entropy flux and the diffusion potential, following de Groot and Mazur (1962), Coleman and Noll (1963) Ammar et al. (2009a) and Villani et al. (2014):

$$\underline{\boldsymbol{\Phi}} = \frac{1}{T}\sum_i \mu_i \underline{\boldsymbol{J}}_i. \tag{22}$$

Expanding Eqs. (20)–(22) and using the mass and energy balance equations (5) and (7) combined with the averaging relations (18) lead to the Clausius–Duhem inequality:

$$-\left(\pi + \frac{\partial f}{\partial \phi}\right)\dot{\phi} + \left(\underline{\boldsymbol{\xi}} - \frac{\partial f}{\partial \nabla\phi}\right)\cdot\nabla\dot{\phi} + \sum_i \mu_i \dot{c}_i - h\frac{\partial f^\alpha}{\partial c_i^\alpha}\dot{c}_i^\alpha - \bar{h}\frac{\partial f^\beta}{\partial c_i^\beta}\dot{c}_i^\beta - \sum_i \underline{\boldsymbol{J}}_i\cdot\nabla\mu_i + \underset{\sim}{\boldsymbol{\sigma}} : \dot{\underset{\sim}{\boldsymbol{\varepsilon}}} - h\frac{\partial f^\alpha}{\partial \underset{\sim}{\boldsymbol{\varepsilon}}_e^{\,\alpha}} : \dot{\underset{\sim}{\boldsymbol{\varepsilon}}}_e^{\,\alpha} - \bar{h}\frac{\partial f^\beta}{\partial \underset{\sim}{\boldsymbol{\varepsilon}}_e^{\,\beta}} : \dot{\underset{\sim}{\boldsymbol{\varepsilon}}}_e^{\,\beta} - \sum_s \bar{h}\frac{\partial f^\beta}{\partial \rho_s^\beta}\dot{\rho}_s^\beta - \sum_s \bar{h}\frac{\partial f^\beta}{\partial x_s^\beta}\dot{x}_s^\beta \geq 0. \tag{23}$$

The previous inequality is first exploited for the individual phases. The particular case $\phi = 1$ corresponds to the pure phase α:

$$\sum_i \left(\mu_i^{\,\alpha} - \frac{\partial f^\alpha}{\partial c_i^\alpha}\right)\dot{c}_i^\alpha - \sum_i \underline{\boldsymbol{J}}_i^{\,\alpha}\cdot\nabla\mu_i^{\,\alpha} + \left(\underset{\sim}{\boldsymbol{\sigma}}^\alpha - \frac{\partial f^\alpha}{\partial \underset{\sim}{\boldsymbol{\varepsilon}}_e^{\,\alpha}}\right) : \dot{\underset{\sim}{\boldsymbol{\varepsilon}}}_e^{\,\alpha} + \underset{\sim}{\boldsymbol{\sigma}}^\alpha : \dot{\underset{\sim}{\boldsymbol{\varepsilon}}}_p^{\,\alpha} \geq 0, \tag{24}$$

whereas the particular case for the phase β, $\phi = 0$, reads:

$$\sum_i \left(\mu_i^{\,\beta} - \frac{\partial f^\beta}{\partial c_i^\beta}\right)\dot{c}_i^\beta - \sum_i \underline{\boldsymbol{J}}_i^{\,\beta}\cdot\nabla\mu_i^{\,\beta} + \left(\underset{\sim}{\boldsymbol{\sigma}}^\beta - \frac{\partial f^\beta}{\partial \underset{\sim}{\boldsymbol{\varepsilon}}_e^{\,\beta}}\right) : \dot{\underset{\sim}{\boldsymbol{\varepsilon}}}_e^{\,\beta} + \underset{\sim}{\boldsymbol{\sigma}}^\beta : \dot{\underset{\sim}{\boldsymbol{\varepsilon}}}_p^{\,\beta} - \sum_s \frac{\partial f^\beta}{\partial \rho_s^\beta}\dot{\rho}_s^\beta - \sum_s \frac{\partial f^\beta}{\partial x_s^\beta}\dot{x}_s^\beta \geq 0. \tag{25}$$

Assuming that the diffusion potentials and the stress tensors do not depend explicitly on $\dot{c}_i^\alpha$, $\dot{c}_i^\beta$, $\dot{\underset{\sim}{\boldsymbol{\varepsilon}}}_e^{\,\alpha}$ and $\dot{\underset{\sim}{\boldsymbol{\varepsilon}}}_e^{\,\beta}$, the left-hand sides of the two previous inequalities are linear forms with respect to the concentration and elastic strain increments. Following Coleman and Noll (1963), their positivity requires that the cofactors must vanish:

$$\mu_i^{\,\alpha} = \frac{\partial f^\alpha}{\partial c_i^\alpha}, \quad \mu_i^{\,\beta} = \frac{\partial f^\beta}{\partial c_i^\beta}, \quad \underset{\sim}{\boldsymbol{\sigma}}^\alpha = \frac{\partial f^\alpha}{\partial \underset{\sim}{\boldsymbol{\varepsilon}}_e^{\,\alpha}}, \quad \underset{\sim}{\boldsymbol{\sigma}}^\beta = \frac{\partial f^\beta}{\partial \underset{\sim}{\boldsymbol{\varepsilon}}_e^{\,\beta}}. \tag{26}$$

The thermodynamic forces associated with the hardening variables are then defined as:

$$R_s^\beta = \frac{\partial f^\beta}{\partial \rho_s^\beta}, \quad X_s^\beta = \frac{\partial f^\beta}{\partial x_s^\beta}. \tag{27}$$

The residual dissipation rate inequality is obtained after combining (23) with (26), (27) and (1):

$$-\pi^\sharp\,\dot{\phi} + \left(\underline{\boldsymbol{\xi}} - \frac{\partial f}{\partial \nabla\phi}\right)\cdot\nabla\dot{\phi} + \sum_i h\left(\mu_i - \mu_i^{\,\alpha}\right)\dot{c}_i^\alpha + \sum_i \bar{h}\left(\mu_i - \mu_i^{\,\beta}\right)\dot{c}_i^\beta - \sum_i \underline{\boldsymbol{J}}_i\cdot\nabla\mu_i + h\left(\underset{\sim}{\boldsymbol{\sigma}} - \underset{\sim}{\boldsymbol{\sigma}}^\alpha\right) : \dot{\underset{\sim}{\boldsymbol{\varepsilon}}}_e^{\,\alpha} + \bar{h}\left(\underset{\sim}{\boldsymbol{\sigma}} - \underset{\sim}{\boldsymbol{\sigma}}^\beta\right) : \dot{\underset{\sim}{\boldsymbol{\varepsilon}}}_e^{\,\beta} + h\underset{\sim}{\boldsymbol{\sigma}} : \dot{\underset{\sim}{\boldsymbol{\varepsilon}}}_p^{\,\alpha} + \bar{h}\underset{\sim}{\boldsymbol{\sigma}} : \dot{\underset{\sim}{\boldsymbol{\varepsilon}}}_p^{\,\beta} - \bar{h}\sum_s R_s^\beta\dot{\rho}_s^\beta - \bar{h}\sum_s X_s^\beta\dot{x}_s^\beta \geq 0, \tag{28}$$

where $\pi^\sharp$ is defined as

$$\pi^\sharp = \pi + \frac{\partial f}{\partial \phi} - h'\left[\sum_i \mu_i\left(c_i^\alpha - c_i^\beta\right) + \underset{\sim}{\boldsymbol{\sigma}} : \left(\underset{\sim}{\boldsymbol{\varepsilon}}^\alpha - \underset{\sim}{\boldsymbol{\varepsilon}}^\beta\right)\right]. \tag{29}$$

and is similar to the dissipative microforce introduced by Gurtin (1996).

At this point, it is still assumed that the diffusion potential and stress tensor functions do not explicitly depend on the rates $\dot{c}_i^\alpha$, $\dot{c}_i^\beta$ and $\dot{\underset{\sim}{\boldsymbol{\varepsilon}}}_e^{\,\alpha}$ and $\dot{\underset{\sim}{\boldsymbol{\varepsilon}}}_e^{\,\beta}$. In that case, it follows that the following conditions must hold to ensure positivity of the dissipation rate:

$$\mu_i = \mu_i^{\,\beta} = \mu_i^{\,\alpha}, \quad \underset{\sim}{\boldsymbol{\sigma}} = \underset{\sim}{\boldsymbol{\sigma}}^\alpha = \underset{\sim}{\boldsymbol{\sigma}}^\beta. \tag{30}$$

The first condition of equal partial diffusion potentials was adopted as a starting point by Kim et al. (1999). The equality of partial stresses associated with each phase at a material point corresponds to the well-known Reuss approximation in the mechanical homogenization theory and was first applied by Steinbach and Apel (2006) and discussed in Ammar et al.

(2009b), Durga et al. (2013) and Mosler et al. (2014).

Finally, following Gurtin (1996), the generalized stress vector $\underline{\boldsymbol{\xi}}$ is assumed to be independent of $\nabla\dot{\phi}$, which provides the last state law:

$$\underline{\boldsymbol{\xi}} = \frac{\partial f}{\partial \nabla \phi}. \tag{31}$$

As a result, the residual dissipation inequality reads:

$$-\pi^{\sharp}\,\dot{\phi} - \underline{\boldsymbol{J}}_{\mathrm{i}}\cdot\nabla\mu_{\mathrm{i}} + h\underset{\sim}{\boldsymbol{\sigma}}\colon \dot{\underset{\sim}{\boldsymbol{\varepsilon}}}_{p}^{\alpha} + \bar{h}\left(\underset{\sim}{\boldsymbol{\sigma}}\colon \dot{\underset{\sim}{\boldsymbol{\varepsilon}}}_{p}^{\beta} - \sum_{s} R_{s}^{\beta}\dot{\rho}_{s}^{\beta} - \sum_{s} X_{s}^{\beta}\dot{x}_{s}^{\beta}\right) \geq 0. \tag{32}$$

The mechanical contributions in the previous inequality contain the plastic power and the possible energy storage by means of increase of internal variables.

At this stage, specific choices for the bulk volumetric free energy densities can be introduced in the form of quadratic potentials for the purpose of illustration. The chemical contributions

$$f_{c_{\mathrm{i}}}^{\psi}(c_{\mathrm{i}}^{\psi}) = \frac{1}{2}\,k_{i}^{\psi}\left(c_{\mathrm{i}}^{\psi} - \hat{c}_{\mathrm{i}}^{\psi}\right)^{2}, \tag{33}$$

correspond to elliptic paraboloids with minimum at $\hat{c}_{i}^{\psi}$ and curvature given by k_{i}^{ψ}. The elasticity contribution for the α phase

$$f_{\varepsilon}^{\alpha}(\underset{\sim}{\boldsymbol{\varepsilon}}_{e}^{\alpha}) = \frac{1}{2}\,\underset{\sim}{\boldsymbol{\varepsilon}}_{e}^{\alpha}\colon \underset{\approx}{\boldsymbol{\Lambda}}^{\alpha}\colon \underset{\sim}{\boldsymbol{\varepsilon}}_{e}^{\alpha}, \tag{34}$$

involves the fourth-order tensor of elastic moduli of the bulk phase, $\underset{\approx}{\boldsymbol{\Lambda}}^{\alpha}$. The energy stored by elasticity and hardening for the phase β is taken from Busso and Cailletaud (2005) and Besson et al. (2009):

$$f_{\varepsilon}^{\beta}(\underset{\sim}{\boldsymbol{\varepsilon}}_{e}^{\beta}) = \frac{1}{2}\,\underset{\sim}{\boldsymbol{\varepsilon}}_{e}^{\beta}\colon \underset{\approx}{\boldsymbol{\Lambda}}^{\beta}\colon \underset{\sim}{\boldsymbol{\varepsilon}}_{e}^{\beta} + \frac{1}{2}\,b^{\beta}Q^{\beta}\sum_{s,r} H^{sr}\rho_{s}^{\beta}\rho_{r}^{\beta} + \frac{1}{2}\,C^{\beta}\sum_{s}\left(x_{s}^{\beta}\right)^{2}. \tag{35}$$

The hardening parameters are Q^{β}, b^{β} and C^{β}. The interaction matrix H^{sr} accounts for self and latent hardening induced by dislocation interactions.

Based on the previous quadratic potentials, the state laws (26), (27) and (31) combined with (30) provide:

$$\mu_{i}^{\psi} = k_{i}^{\psi}\left(c_{i}^{\psi} - \hat{c}_{i}^{\psi}\right) = \mu_{i}, \tag{36}$$

along with

$$\underset{\sim}{\boldsymbol{\sigma}}^{\psi} = \underset{\approx}{\boldsymbol{\Lambda}}^{\psi}\colon \underset{\sim}{\boldsymbol{\varepsilon}}_{e}^{\psi} = \underset{\sim}{\boldsymbol{\sigma}}, \tag{37}$$

$$R_{s}^{\beta} = b^{\beta}Q^{\beta}\sum_{r} H^{sr}\rho_{r}^{\beta}, \quad X_{s}^{\beta} = C^{\beta}x_{s}^{\beta}. \tag{38}$$

The generalized stress vector is proportional to the gradient of the phase field variable, following (15) and (31):

$$\underline{\boldsymbol{\xi}} = 6\gamma\lambda\,\nabla\phi. \tag{39}$$

3.4. Constitutive laws from the dissipation potential

The positivity of the dissipation rate in (32) can be identically fulfilled by introducing a convex dissipation potential depending on the generalized stresses, conjugate to the flow of phase field, concentration, plastic strain and hardening variables:

$$\Omega = \Omega(\pi^{\sharp},\ \nabla\mu_{\mathrm{i}}^{\alpha}, \nabla\mu_{\mathrm{i}}^{\beta},\ \underset{\sim}{\boldsymbol{\sigma}}^{\alpha}, \underset{\sim}{\boldsymbol{\sigma}}^{\beta}, R_{s}^{\beta}, X_{s}^{\beta};\ \phi). \tag{40}$$

The dissipation potential Ω is a function of thermodynamic forces and may also depend on the thermodynamic variables that have to be considered as parameters, according to Germain et al. (1983). Here ϕ is used in the decomposition of the dissipation potential in weighted contributions of the individual phases, as done for the free energy density function:

$$\Omega = \Omega_{\pi}(\pi^{\sharp}) + h(\phi)\Omega^{\alpha}(\nabla\mu_{\mathrm{i}}^{\alpha}, \underset{\sim}{\boldsymbol{\sigma}}^{\alpha}) + \bar{h}(\phi)\Omega^{\beta}(\nabla\mu_{\mathrm{i}}^{\beta}, \underset{\sim}{\boldsymbol{\sigma}}^{\beta}, R_{s}^{\beta}, X_{s}^{\beta}). \tag{41}$$

Looking at (24)–(27), quadratic dissipation potentials can be chosen in the form:

$$\begin{cases} \Omega_\pi(\pi^\sharp) = M_\phi \pi^{\sharp 2}, & (42) \\ \Omega^\alpha(\nabla\mu_i^\alpha, \underset{\sim}{\sigma}^\alpha) = \frac{1}{2} M_i^\alpha |\nabla\mu_i^\alpha|^2 + \frac{K^\alpha}{n^\alpha+1} \left\langle \frac{\sqrt{3/2\ \underset{\sim}{\sigma}^\alpha_{\text{dev}} : \underset{\sim}{\sigma}^\alpha_{\text{dev}}} - R_0^\alpha}{K^\alpha} \right\rangle^{n^\alpha+1}, & (43) \\ \Omega^\beta(\nabla\mu_i^\beta, \underset{\sim}{\sigma}^\beta, R_s^\beta, X_s^\beta) = \frac{1}{2} M_i^\beta |\nabla\mu_i^\beta|^2 + \frac{K^\beta}{n^\beta+1} \sum_s \left\langle \frac{|\underset{\sim}{\sigma}^\beta : \underset{\sim}{\boldsymbol{m}}_s^\beta - X_s^\beta| - R_0^\beta - R_s^\beta}{K^\beta} \right\rangle^{n^\beta+1}. & (44) \end{cases}$$

M_ϕ and M_i^ψ are the mobility parameters respectively for the phase-field and diffusion in phase ψ. For simplicity, cross terms between the different species are not considered (the matrix of mobility is diagonal) and the mobilities are taken isotropic. The brackets $\langle . \rangle$ denote the Macaulay brackets, they deliver the positive part of the concerned quantity. A von Mises yield criterion with constant threshold R_0^α is chosen for the α phase whereas the Schmid law is adopted in the β phase, R_0^β being the initial critical resolved shear stress and R_s^β the hardening variable for each slip system. The deviatoric stress tensors are called $\underset{\sim}{\sigma}^\psi_{\text{dev}}$. The crystallographic orientation tensor $\underset{\sim}{\boldsymbol{m}}_s^\beta$ is the tensor product of the slip direction and normal to the slip plane for slip system s, see Asaro and Lubarda (2006). The material parameters K^ψ and n^ψ account for the generally nonlinear viscous properties of both phases.

The dissipation potential is used to derive the flow rules for diffusion and viscoplasticity. The mass flux vectors present in the Clausius–Duhem inequalities obtained in (24) and (25) are derived from the dissipation potential for $\phi = 1$ and $\phi = 0$ as follows:

$$\underline{\boldsymbol{J}}_i^\alpha = -\frac{\partial\Omega^\alpha}{\partial\nabla\mu_i^\alpha} = -M_i^\alpha \nabla\mu_i^\alpha, \quad \underline{\boldsymbol{J}}_i^\beta = -\frac{\partial\Omega^\beta}{\partial\nabla\mu_i^\beta} = -M_i^\beta \nabla\mu_i^\beta \tag{45}$$

where the diffusion mobilities L_i^ψ can be related to the diffusivities D_i^ψ as follows, in order to retrieve the generalized Fick law of diffusion:

$$L_i^\psi = D_i^\psi \left(\frac{\partial^2 f^\psi}{\partial c_i^{\psi 2}} \right)^{-1}. \tag{46}$$

Using then the flux averaging relations (1) and (30), one obtains:

$$\underline{\boldsymbol{J}}_i = -\left(h(\phi) L_i^\alpha + \bar{h}(\phi) L_i^\beta \right) \nabla\mu_i, \tag{47}$$

so that effective mobilities can be defined as the average of the bulk diffusivities of the phases:

$$L_i(\phi) = h(\phi) L_i^\alpha + \bar{h}(\phi) L_i^\beta. \tag{48}$$

The plastic flow and hardening rules can also be derived from the dissipation potential following the theory of standard generalized materials (Besson et al., 2009):

$$\underset{\sim}{\dot{\boldsymbol{\varepsilon}}}_p^\alpha = \frac{\partial\Omega_p^\alpha}{\partial\underset{\sim}{\sigma}^\alpha} = \left\langle \frac{\sqrt{3/2\ \underset{\sim}{\sigma}^\alpha_{\text{dev}} : \underset{\sim}{\sigma}^\alpha_{\text{dev}}} - R_0^\alpha}{K^\alpha} \right\rangle^{n^\alpha} \frac{3/2\ \underset{\sim}{\sigma}^\alpha_{\text{dev}}}{\sqrt{3/2,\ \underset{\sim}{\sigma}^\alpha_{\text{dev}} : \underset{\sim}{\sigma}^\alpha_{\text{dev}}}}. \tag{49}$$

This corresponds to usual von Mises power-law viscoplasticity with threshold R_0^α. As for the phase β:

$$\underset{\sim}{\dot{\boldsymbol{\varepsilon}}}_p^\beta = \frac{\partial\Omega_p^\beta}{\partial\underset{\sim}{\sigma}^\beta} = \sum_s \left\langle \frac{|\underset{\sim}{\sigma}^\beta : \underset{\sim}{\boldsymbol{m}}_s^\beta - X_s^\beta| - R_s^\beta}{K} \right\rangle^{n^\beta} \underset{\sim}{\boldsymbol{m}}_s^\beta \operatorname{sign}\left(\underset{\sim}{\sigma}^\beta : \underset{\sim}{\boldsymbol{m}}_s^\beta - X_s^\beta \right) = \sum_s \dot{\gamma}_s \underset{\sim}{\boldsymbol{m}}_s^\beta, \tag{50}$$

where $\dot{\gamma}_\alpha$ is the slip rate for the slip system number s. The double contraction of the stress tensor $\underset{\sim}{\sigma}^\beta$ and the orientation $\underset{\sim}{\boldsymbol{m}}_s^\beta$ is called the resolved shear stress on slip system s and is the driving force for slip activation in the presence of a back-stress X_s^β.

The evolution laws for nonlinear hardening are defined following Busso and Cailletaud (2005) and Besson et al. (2009):

$$\dot{\rho}_s^\beta = \left(1 - b^\beta \rho_s^\beta\right) |\dot{\gamma}_s|, \quad \dot{x}_s^\beta = \left(\operatorname{sign}(\underset{\sim}{\sigma}^\beta : \underset{\sim}{\boldsymbol{m}}_s^\beta - X_s^\beta) - d^\beta x_s^\beta \right) |\dot{\gamma}_s|. \tag{51}$$

More sophisticated evolution laws like Kocks–Mecking equations for the dislocation densities can be used in the model, instead of $(51)_1$.

Finally, the evolution of the phase field variable is derived from the quadratic part of the dissipation potential depending on $\pi^\sharp$ as follows:

$$\dot{\phi} = -\frac{\partial\Omega}{\partial\pi^\sharp} = -M_\phi \pi^\sharp. \tag{52}$$

The latter equation can be reformulated into the well-known Allen–Cahn equation by introducing the generalized stress

balance equation (8) and the state law (31) combined with (29):

$$\frac{\dot{\phi}}{M_\phi} = 6\gamma\lambda\,\Delta\phi - \frac{\partial f}{\partial \phi} + h'\left[\sum_i \mu_i\left(c_i^\alpha - c_i^\beta\right) + \underset{\sim}{\boldsymbol{\sigma}}\colon\left(\underset{\sim}{\boldsymbol{\varepsilon}}^\alpha - \underset{\sim}{\boldsymbol{\varepsilon}}^\beta\right)\right]. \tag{53}$$

It is convenient to rewrite the enhanced Allen–Cahn equation (53) by introducing F_ϕ^R as follows:

$$\frac{\dot{\phi}}{M_\phi} = 3\gamma\left(2\lambda\,\Delta\phi - \frac{1}{\lambda}W'\right) - h'F_\phi^R, \tag{54}$$

where

$$F_\phi^R = f^\alpha - f^\beta - \sum_i \mu_i\left(c_i^\alpha - c_i^\beta\right) - \underset{\sim}{\boldsymbol{\sigma}}\colon\left(\underset{\sim}{\boldsymbol{\varepsilon}}^\alpha - \underset{\sim}{\boldsymbol{\varepsilon}}^\beta\right). \tag{55}$$

It can be noted that when $F_\phi^R = 0$ the equilibrium condition in Frolov and Mishin (2012) Eq. (29) is recovered, see also Spatschek and Eidel (2013). The above constitutive laws are then consistent with a positive dissipation rate at each material point and at each time. Note that Eq. (55) is valid for any form of the free energy function. In the particular case of quadratic elastic and chemical potentials, Eq. (55) becomes:

$$F_\phi^R = -\frac{1}{2}\sum_i \mu_i\left(c_i^\alpha - c_i^\beta\right) - \frac{1}{2}\underset{\sim}{\boldsymbol{\sigma}}\colon\left(\underset{\sim}{\boldsymbol{\varepsilon}}^\alpha - \underset{\sim}{\boldsymbol{\varepsilon}}^\beta\right). \tag{56}$$

4. Constitutive framework based on the Gibbs free energy potential

It has been shown in Section 3 that the restrictions implied by the entropy principle on the form of the constitutive and state laws based on the homogenization approach from the volumetric free energy density have lead us to select the Reuss homogenization scheme regarding stresses and diffusion potentials attached to each phase at each material point. Following a similar reasoning as in Plapp (2011), an alternative formulation is put forward in this section, based on the use of the Gibbs free energy or free enthalpy that will prompt us to introduce an alternative homogenization scheme for the mechanical part of the model. The volumetric Gibbs energy density function g is defined as the double Legendre transform of the volumetric internal energy density e:

$$g = e - Ts - \underset{\sim}{\boldsymbol{\sigma}}\colon\underset{\sim}{\boldsymbol{\varepsilon}}. \tag{57}$$

4.1. State and internal variables

While entropy and strain are the canonical variables of the internal energy density function, temperature and stress are the arguments of the free enthalpy. Accordingly, the state space (12) designed for the Helmholtz free energy must be modified into:

$$\text{STATE} = \{\phi,\ \nabla\phi,\ c_i^\alpha,\ \underset{\sim}{\boldsymbol{\sigma}}^\alpha,\ \underset{\sim}{\boldsymbol{\varepsilon}}_p^\alpha,\ c_i^\beta,\ \underset{\sim}{\boldsymbol{\sigma}}^\beta,\ \underset{\sim}{\boldsymbol{\varepsilon}}_p^\beta,\ \rho_s^\beta,\ x_s^\beta\}, \tag{58}$$

where the plastic strain tensors $\underset{\sim}{\boldsymbol{\varepsilon}}_p^w$ enter as internal variables, together with the hardening variables already introduced in (12) for reasons that will become apparent in the sequel.

4.2. Partition of the Gibbs energy density function

The volumetric free enthalpy density g is decomposed into interface, chemical and mechanical parts, respectively g_ϕ, g_{c_i} and g_σ as follows:

$$g = g_\phi(\phi, \nabla\phi) + g_{c_i}(\phi, c_i^\alpha, c_i^\beta) + g_\sigma(\phi, \underset{\sim}{\boldsymbol{\sigma}}^\alpha, \underset{\sim}{\boldsymbol{\varepsilon}}_p^\alpha, \underset{\sim}{\boldsymbol{\sigma}}^\beta, \underset{\sim}{\boldsymbol{\varepsilon}}_p^\beta, \rho_s^\beta, x_s^\beta), \tag{59}$$

where the diffuse interface excess enthalpy g_ϕ is identical to (15).

Bulk free energies are coupled by means of the phase field variable using the same averaging rules as used for the state variables, thermodynamic forces and fluxes (1):

$$g_{c_i}(\phi, c_i^\alpha, c_i^\beta) = h(\phi)g_{c_i}^\alpha(c_i^\alpha) + \overline{h}(\phi)g_{c_i}^\beta(c_i^\beta), \tag{60}$$

$$g_\sigma(\phi, \underset{\sim}{\boldsymbol{\sigma}}^\alpha, \underset{\sim}{\boldsymbol{\sigma}}^\beta, \underset{\sim}{\boldsymbol{\varepsilon}}_p^\beta, \rho_s^\beta, x_\alpha^\beta) = h(\phi)g_\sigma^\alpha(\underset{\sim}{\boldsymbol{\sigma}}^\alpha, \underset{\sim}{\boldsymbol{\varepsilon}}_p^\alpha) + \overline{h}(\phi)g_\sigma^\beta(\underset{\sim}{\boldsymbol{\sigma}}^\beta, \underset{\sim}{\boldsymbol{\varepsilon}}_p^\beta, \rho_s^\beta, x_\alpha^\beta). \tag{61}$$

4.3. State laws

The time derivative of (57), considering an isothermal thermodynamic process, is used now to rewrite the second law of thermodynamics (19) as:

$$\dot{e} - \dot{g} - \underset{\sim}{\boldsymbol{\sigma}}: \dot{\underset{\sim}{\boldsymbol{\varepsilon}}} - \underset{\sim}{\boldsymbol{\varepsilon}}: \dot{\underset{\sim}{\boldsymbol{\sigma}}} \geq T\, \nabla\cdot\underline{\underline{\boldsymbol{\Phi}}}. \tag{62}$$

Taking the local energy balance equation (7) into account leads to the following expression:

$$-\underset{\sim}{\boldsymbol{\varepsilon}}: \dot{\underset{\sim}{\boldsymbol{\sigma}}} - \pi\dot{\phi} + \underline{\boldsymbol{\xi}}\cdot\nabla\dot{\phi} - \dot{g} \geq T\, \nabla\cdot\underline{\underline{\boldsymbol{\Phi}}} \tag{63}$$

where the stress rate tensor $\dot{\underset{\sim}{\boldsymbol{\sigma}}}$ can be expanded into:

$$\dot{\underset{\sim}{\boldsymbol{\sigma}}} = h(\phi)\, \dot{\underset{\sim}{\boldsymbol{\sigma}}}^{\alpha} + \bar{h}(\phi)\, \dot{\underset{\sim}{\boldsymbol{\sigma}}}^{\beta} + h'(\phi)\dot{\phi}\left(\underset{\sim}{\boldsymbol{\sigma}}^{\alpha} - \underset{\sim}{\boldsymbol{\sigma}}^{\beta}\right). \tag{64}$$

Using the expression (22) for the entropy flux and the chain rule for g, the inequality (63) becomes:

$$\begin{aligned} -\pi^{*}\dot{\phi} + \left(\underline{\boldsymbol{\xi}} - \frac{\partial g}{\partial \nabla\phi}\right)\cdot\nabla\dot{\phi} + h\sum_i\left(\mu_{\mathrm{i}} - \frac{\partial g^{\alpha}}{\partial c_{\mathrm{i}}^{\alpha}}\right)\dot{c}_{\mathrm{i}}^{\alpha} + \bar{h}\sum_i\left(\mu_{\mathrm{i}} - \frac{\partial g^{\beta}}{\partial c_{\mathrm{i}}^{\beta}}\right)\dot{c}_{\mathrm{i}}^{\beta} - \sum_i \underline{\boldsymbol{J}}_{\mathrm{i}}\cdot\nabla\mu_{\mathrm{i}} - h\left[\left(\underset{\sim}{\boldsymbol{\varepsilon}} + \frac{\partial g^{\alpha}}{\partial \underset{\sim}{\boldsymbol{\sigma}}^{\alpha}}\right): \dot{\underset{\sim}{\boldsymbol{\sigma}}}^{\alpha} + \frac{\partial g^{\alpha}}{\partial \underset{\sim}{\boldsymbol{\varepsilon}}_p^{\alpha}}: \dot{\underset{\sim}{\boldsymbol{\varepsilon}}}_p^{\alpha}\right] \\ - \bar{h}\left[\left(\underset{\sim}{\boldsymbol{\varepsilon}} + \frac{\partial g^{\beta}}{\partial \underset{\sim}{\boldsymbol{\sigma}}^{\beta}}\right): \dot{\underset{\sim}{\boldsymbol{\sigma}}}^{\beta} + \frac{\partial g^{\beta}}{\partial \underset{\sim}{\boldsymbol{\varepsilon}}_p^{\beta}}: \dot{\underset{\sim}{\boldsymbol{\varepsilon}}}_p^{\beta} + \sum_s \frac{\partial g^{\beta}}{\partial \rho_s^{\beta}}\dot{\rho}_s^{\beta} + \sum_s \frac{\partial g^{\beta}}{\partial x_s^{\beta}}\dot{x}_s^{\beta}\right] \geq 0, \end{aligned} \tag{65}$$

where

$$\pi^{*} = \pi + \frac{\partial g}{\partial \phi} - h'(\phi)\left[\sum_i \mu_{\mathrm{i}}\left(c_{\mathrm{i}}^{\alpha} - c_{\mathrm{i}}^{\beta}\right) - \underset{\sim}{\boldsymbol{\varepsilon}}: \left(\underset{\sim}{\boldsymbol{\sigma}}^{\alpha} - \underset{\sim}{\boldsymbol{\sigma}}^{\beta}\right)\right]. \tag{66}$$

The particular case $\phi = 1$ corresponding to the pure phase α yields:

$$\sum_i\left(\mu_{\mathrm{i}}^{\alpha} - \frac{\partial g^{\alpha}}{\partial c_{\mathrm{i}}^{\alpha}}\right)\dot{c}_{\mathrm{i}}^{\alpha} - \sum_i \underline{\boldsymbol{J}}_{\mathrm{i}}^{\alpha}\cdot\nabla\mu_{\mathrm{i}}^{\alpha} - \left(\underset{\sim}{\boldsymbol{\varepsilon}}^{\alpha} + \frac{\partial g^{\alpha}}{\partial \underset{\sim}{\boldsymbol{\sigma}}^{\alpha}}\right): \dot{\underset{\sim}{\boldsymbol{\sigma}}}^{\alpha} - \frac{\partial g^{\alpha}}{\partial \underset{\sim}{\boldsymbol{\varepsilon}}_p^{\alpha}}: \dot{\underset{\sim}{\boldsymbol{\varepsilon}}}_p^{\alpha} \geq 0. \tag{67}$$

The particular case $\phi = 0$ corresponding to the pure phase β yields:

$$\sum_i\left(\mu_{\mathrm{i}}^{\beta} - \frac{\partial g^{\beta}}{\partial c_{\mathrm{i}}^{\beta}}\right)\dot{c}_{\mathrm{i}}^{\beta} - \sum_i \underline{\boldsymbol{J}}_{\mathrm{i}}^{\beta}\cdot\nabla\mu_{\mathrm{i}}^{\beta} - \left(\underset{\sim}{\boldsymbol{\varepsilon}}^{\beta} + \frac{\partial g^{\beta}}{\partial \underset{\sim}{\boldsymbol{\sigma}}^{\beta}}\right): \dot{\underset{\sim}{\boldsymbol{\sigma}}}^{\beta} - \frac{\partial g^{\beta}}{\partial \underset{\sim}{\boldsymbol{\varepsilon}}_p^{\beta}}: \dot{\underset{\sim}{\boldsymbol{\varepsilon}}}_p^{\beta} - \sum_s \frac{\partial g^{\beta}}{\partial \rho_s^{\beta}}\dot{s}_{\alpha}^{\beta} - \sum_s \frac{\partial g^{\beta}}{\partial x_s^{\beta}}\dot{x}_s^{\beta} \geq 0. \tag{68}$$

The found dissipation rate is a linear form with respect to $\dot{c}_{\mathrm{i}}^{\alpha}$, $\dot{c}_{\mathrm{i}}^{\beta}$ and $\dot{\underset{\sim}{\boldsymbol{\sigma}}}^{\alpha}$ and $\dot{\underset{\sim}{\boldsymbol{\sigma}}}^{\beta}$. The positivity of dissipation rate then requires that the conjugate quantities must vanish in both cases (67) and (68):

$$\mu_{\mathrm{i}}^{\alpha} = \frac{\partial g^{\alpha}}{\partial c_{\mathrm{i}}^{\alpha}}, \quad \mu_{\mathrm{i}}^{\beta} = \frac{\partial g^{\beta}}{\partial c_{\mathrm{i}}^{\beta}}, \quad \underset{\sim}{\boldsymbol{\varepsilon}}^{\alpha} = -\frac{\partial g^{\alpha}}{\partial \underset{\sim}{\boldsymbol{\sigma}}^{\alpha}}, \quad \underset{\sim}{\boldsymbol{\varepsilon}}^{\beta} = -\frac{\partial g^{\beta}}{\partial \underset{\sim}{\boldsymbol{\sigma}}^{\beta}}, \tag{69}$$

and by definition:

$$R_s^{\beta} = -\frac{\partial g^{\beta}}{\partial \rho_s^{\beta}}, \quad X_s^{\beta} = -\frac{\partial g^{\beta}}{\partial x_s^{\beta}}, \quad \underset{\sim}{\boldsymbol{\sigma}}^{\alpha} = -\frac{\partial g^{\alpha}}{\partial \underset{\sim}{\boldsymbol{\varepsilon}}_p^{\alpha}}, \quad \underset{\sim}{\boldsymbol{\sigma}}^{\beta} = -\frac{\partial g^{\beta}}{\partial \underset{\sim}{\boldsymbol{\varepsilon}}_p^{\beta}}. \tag{70}$$

The two last conditions are required for the plastic power to appear in the dissipation rate.

Returning to the general case, given by (65), and using the mixture rules (1) and the state laws (69) and (70), the dissipation rate inequality becomes:

$$\begin{aligned} -\pi^{*}\dot{\phi} + \left(\underline{\boldsymbol{\xi}} - \frac{\partial g}{\partial \nabla\phi}\right)\cdot\nabla\dot{\phi} + h\sum_i(\mu_{\mathrm{i}} - \mu_{\mathrm{i}}^{\alpha})\dot{c}_{\mathrm{i}}^{\alpha} + \bar{h}\sum_i(\mu_{\mathrm{i}} - \mu_{\mathrm{i}}^{\beta})\dot{c}_{\mathrm{i}}^{\beta} - \sum_i \underline{\boldsymbol{J}}_{\mathrm{i}}\cdot\nabla\mu_{\mathrm{i}} - h\left[(\underset{\sim}{\boldsymbol{\varepsilon}} - \underset{\sim}{\boldsymbol{\varepsilon}}^{\alpha}): \dot{\underset{\sim}{\boldsymbol{\sigma}}}^{\alpha} - \underset{\sim}{\boldsymbol{\sigma}}^{\alpha}: \dot{\underset{\sim}{\boldsymbol{\varepsilon}}}_p^{\alpha}\right] \\ - \bar{h}\left[(\underset{\sim}{\boldsymbol{\varepsilon}} - \underset{\sim}{\boldsymbol{\varepsilon}}^{\beta}): \dot{\underset{\sim}{\boldsymbol{\sigma}}}^{\beta} - \underset{\sim}{\boldsymbol{\sigma}}^{\beta}: \dot{\underset{\sim}{\boldsymbol{\varepsilon}}}_p^{\beta} + \sum_s R_s^{\beta}\dot{\rho}_s^{\beta} + \sum_s X_s^{\beta}\dot{x}_s^{\beta}\right] \geq 0. \end{aligned} \tag{71}$$

Additional conditions result from the fact that the previous dissipation rate is a positive linear form with respect to $\dot{c}_{\mathrm{i}}^{\alpha}$, $\dot{c}_{\mathrm{i}}^{\beta}$ and $\dot{\underset{\sim}{\boldsymbol{\sigma}}}^{\alpha}$ and $\dot{\underset{\sim}{\boldsymbol{\sigma}}}^{\beta}$:

$$\mu_{\mathrm{i}} = \mu_{\mathrm{i}}^{\beta} = \mu_{\mathrm{i}}^{\alpha}, \quad \underset{\sim}{\boldsymbol{\varepsilon}} = \underset{\sim}{\boldsymbol{\varepsilon}}^{\alpha} = \underset{\sim}{\boldsymbol{\varepsilon}}^{\beta}. \tag{72}$$

The latter strain relations correspond to the Voigt approximation in homogenization theory. Taking these relations into account and keeping the state law (52) for the gradient of the phase field, the following residual dissipation is obtained from

(71):

$$-\pi^*\dot{\phi} - \sum_i \underline{\boldsymbol{J}}_i \cdot \nabla\mu_i + h\, \underset{\sim}{\boldsymbol{\sigma}}^{\alpha} : \dot{\underset{\sim}{\boldsymbol{\varepsilon}}}_p^{\alpha} + \bar{h}\left[\underset{\sim}{\boldsymbol{\sigma}}^{\beta} : \dot{\underset{\sim}{\boldsymbol{\varepsilon}}}_p^{\beta} - \sum_s R_s^{\beta}\dot{\rho}_s^{\beta} - \sum_s X_s^{\beta}\dot{x}_s^{\beta} \right] \geq 0. \tag{73}$$

It differs from Eq. (32) by the contribution $\pi^* \neq \pi^\sharp$.

At this stage, specific choices for the free enthalpy potentials are presented as an illustration of possible constitutive equations within the proposed framework. The following quadratic potentials are retained:

$$g_{c_i}^{\psi}(c_i^{\psi}) = \frac{1}{2} k_i^{\psi}\left(c_i^{\psi} - \hat{c}_i^{\psi}\right)^2, \tag{74}$$

$$g_{\sigma}^{\alpha}(\underset{\sim}{\boldsymbol{\sigma}}^{\alpha}, \underset{\sim}{\boldsymbol{\varepsilon}}_p^{\alpha},) = -\frac{1}{2}\underset{\sim}{\boldsymbol{\sigma}}^{\alpha} : \underset{\approx}{\boldsymbol{S}}^{\alpha} : \underset{\sim}{\boldsymbol{\sigma}}^{\alpha} - \underset{\sim}{\boldsymbol{\sigma}}^{\alpha} : \underset{\sim}{\boldsymbol{\varepsilon}}_{\star}^{\alpha} - \underset{\sim}{\boldsymbol{\sigma}}^{\alpha} : \underset{\sim}{\boldsymbol{\varepsilon}}_p^{\alpha}, \tag{75}$$

$$g_{\sigma}^{\beta}(\underset{\sim}{\boldsymbol{\sigma}}^{\beta}, \underset{\sim}{\boldsymbol{\varepsilon}}_p^{\beta}, s_{\alpha}^{\beta}, b_{\alpha}^{\beta}) = -\frac{1}{2}\underset{\sim}{\boldsymbol{\sigma}}^{\beta} : \underset{\approx}{\boldsymbol{S}}^{\beta} : \underset{\sim}{\boldsymbol{\sigma}}^{\beta} - \underset{\sim}{\boldsymbol{\sigma}}^{\beta} : \underset{\sim}{\boldsymbol{\varepsilon}}_{\star}^{\beta} - \underset{\sim}{\boldsymbol{\sigma}}^{\beta} : \underset{\sim}{\boldsymbol{\varepsilon}}_p^{\beta} - \frac{1}{2} b^{\beta} Q^{\beta} \sum_{sr} H^{sr} \rho_s^{\beta} \rho_r^{\beta} - \frac{1}{2} C^{\beta} \sum_s \left(x_s^{\beta}\right)^2. \tag{76}$$

The chemical potentials are still given by the relations (36), whereas (37) is changed into:

$$\underset{\sim}{\boldsymbol{\varepsilon}}^{\psi} = -\frac{\partial g_{\sigma}^{\psi}}{\partial \underset{\sim}{\boldsymbol{\sigma}}^{\psi}} = \underset{\approx}{\boldsymbol{S}}^{\psi} : \underset{\sim}{\boldsymbol{\sigma}}^{\psi} + \underset{\sim}{\boldsymbol{\varepsilon}}_p^{\psi} + \underset{\sim}{\boldsymbol{\varepsilon}}_{\star}^{\psi} = \underset{\sim}{\boldsymbol{\varepsilon}}, \tag{77}$$

and (38) also remains unchanged.

4.4. Constitutive laws from the dissipation potential

Positivity of the residual dissipation rate can be ensured by choosing a convex dissipation potential Ω^* depending on the generalized forces associated with the flow of phase field, mass and plastic strain:

$$\Omega^* = \Omega^*(\pi^*, \nabla\mu_i^{\alpha}, \nabla\mu_i^{\beta}, \dot{\underset{\sim}{\boldsymbol{\varepsilon}}}_p^{\alpha}, \dot{\underset{\sim}{\boldsymbol{\varepsilon}}}_p^{\beta}, R_s^{\beta}, X_s^{\beta}; \phi). \tag{78}$$

The chosen dissipation potential contains contributions from the diffuse interface and from the individual phase dissipative behavior:

$$\Omega^* = \Omega_{\phi}^*(\pi^*) + h(\phi)\Omega^{*\alpha}(\nabla\mu_i^{\alpha}, \dot{\underset{\sim}{\boldsymbol{\varepsilon}}}_p^{\alpha}) + \bar{h}(\phi)\Omega^{*\beta}(\nabla\mu_i^{\beta}, \dot{\underset{\sim}{\boldsymbol{\varepsilon}}}_p^{\beta}, R_s^{\beta}, X_s^{\beta}). \tag{79}$$

Quadratic individual potentials are chosen for as many physical mechanisms as possible including diffuse interface mobility and bulk diffusion:

$$\begin{cases} \Omega_{\pi}^*(\pi^*) = M_{\phi}\pi^{*2}, \\ \Omega^{*\alpha}(\nabla\mu_i^{\alpha}, \dot{\underset{\sim}{\boldsymbol{\varepsilon}}}_p^{\alpha}) = \dfrac{1}{2} L_i^{\alpha} |\nabla\mu_i^{\alpha}|^2 + \Omega_{\tilde{p}}^{*\alpha}(\dot{\underset{\sim}{\boldsymbol{\varepsilon}}}_p^{\alpha}), \\ \Omega^{*\beta}(\nabla\mu_i^{\beta}, \dot{\underset{\sim}{\boldsymbol{\varepsilon}}}_p^{\beta}, R_s^{\beta}, X_s^{\beta}) = \dfrac{1}{2} L_i^{\beta} |\nabla\mu_i^{\beta}|^2 + \Omega_{\tilde{p}}^{*\beta}(\dot{\underset{\sim}{\boldsymbol{\varepsilon}}}_p^{\beta}, R_s^{\beta}, X_s^{\beta}). \end{cases}$$

The constitutive laws for diffusion are the same as in Section 3.4.

The non-quadratic viscoplastic potential $\Omega_{\tilde{p}}^{*\psi}$ is the dual potential to (44). It is obtained by a Legendre transform of Ω_p^{ψ} from (40) according to Halphen and Nguyen (1975) Eq. (20). The dual potential provides the stress as the derivative with respect to plastic strain rate:

$$\underset{\sim}{\boldsymbol{\sigma}}^{\alpha} = \frac{\partial \Omega_{\tilde{p}}^{*\alpha}}{\partial \dot{\underset{\sim}{\boldsymbol{\varepsilon}}}_p^{\alpha}}, \quad \underset{\sim}{\boldsymbol{\sigma}}^{\beta} = \frac{\partial \Omega_{\tilde{p}}^{*\beta}}{\partial \dot{\underset{\sim}{\boldsymbol{\varepsilon}}}_p^{\beta}}. \tag{83}$$

The hardening laws (51) are still in use in the present context.

Regarding phase transformation, the evolution law for the phase field parameter reads:

$$\dot{\phi} = -\frac{\partial \Omega^*}{\partial \pi^*} = -M_{\phi}\pi^*, \tag{84}$$

where M_{ϕ} is the phase field mobility. The new form of the enhanced Allen–Cahn equation is obtained after substituting (5) and (31) in the latter evolution equation, as:

$$\frac{\dot{\phi}}{M_{\phi}} = 3\gamma\frac{\delta}{z}\Delta\phi - \frac{\partial g}{\partial \phi} + h'\left[\mu_i\left(\sum_i c_i^{\alpha} - c_i^{\beta}\right) - \underset{\sim}{\boldsymbol{\varepsilon}} : \left(\underset{\sim}{\boldsymbol{\sigma}}^{\alpha} - \underset{\sim}{\boldsymbol{\sigma}}^{\beta}\right)\right]. \tag{85}$$

The generalized Allen–Cahn equation (85) can also be rewritten by introducing F_ϕ^V, the counterpart of (54) in Reuss scheme, which reads:

$$F_\phi^V = g^\alpha - g^\beta - \mu_i\left(c_i^\alpha - c_i^\beta\right) + \underset{\sim}{\boldsymbol{\varepsilon}}\colon\left(\underset{\sim}{\boldsymbol{\sigma}}^\alpha - \underset{\sim}{\boldsymbol{\sigma}}^\beta\right). \tag{86}$$

It can be rewritten in terms of Helmholtz's free energy as follows:

$$F_\phi^V = f^\alpha - f^\beta - \mu_i\left(c_i^\alpha - c_i^\beta\right), \tag{87}$$

to be compared with (55) obtained from the Reuss homogenization scheme.

It is worth noting that prior to the choice of a specific homogenization scheme, the equivalence of both models is not ensured. Indeed, if we introduce the Legendre transformation from the Helmholtz to the Gibbs free energy densities for any two phased system:

$$g = f - \underset{\sim}{\boldsymbol{\sigma}}\colon\underset{\sim}{\boldsymbol{\varepsilon}}, \tag{88}$$

Applying the mixture rules (1) to the strain and stress tensors in the previous expression gives:

$$g = f - \left[h(\phi)\underset{\sim}{\boldsymbol{\sigma}}^\alpha + \bar{h}(\phi)\underset{\sim}{\boldsymbol{\sigma}}^\beta\right]\colon\left[h(\phi)\underset{\sim}{\boldsymbol{\varepsilon}}^\alpha + \bar{h}(\phi)\underset{\sim}{\boldsymbol{\varepsilon}}^\beta\right]. \tag{89}$$

On the other hand, for each phase, the bulk free enthalpy can also be expressed as:

$$g^\psi = f^\psi - \underset{\sim}{\boldsymbol{\sigma}}^\psi\colon\underset{\sim}{\boldsymbol{\varepsilon}}^\psi. \tag{90}$$

If we apply (90) into the second model based on the interpolation of the bulk Gibbs energies, it comes that:

$$g = h(\phi)g^\alpha + \bar{h}(\phi)g^\beta \tag{91}$$

$$g = h(\phi)f^\alpha + \bar{h}(\phi)f^\beta - \left[h(\phi)\underset{\sim}{\boldsymbol{\sigma}}^\alpha\colon\underset{\sim}{\boldsymbol{\varepsilon}}^\alpha + \bar{h}(\phi)\underset{\sim}{\boldsymbol{\sigma}}^\beta\colon\underset{\sim}{\boldsymbol{\varepsilon}}^\beta\right] \tag{92}$$

Table 1
Dimensionless material parameters.

Chemical equilibrium		
	Equilibrium concentration $\hat{c}^\alpha$	1
	Equilibrium concentration $\hat{c}^\beta$	0
	Curvature $\tilde{k}^\alpha$	100
	Curvature $\tilde{k}^\beta$	1
Interface properties		
	Interface energy $\tilde{\gamma}$	0.02
Interface thickness $\tilde{\delta}$	Planar precipitates	[0.005; 0.025]
	Circular precipitates	0.025
Mobilities		
	Diffusivity $\tilde{D}^\alpha$	8×10^{-3}
	Diffusivity $\tilde{D}^\beta$	1
	Phase field mobility $\tilde{M}_\phi$	6.17×10^{6}
Elasticity		
	$\varepsilon^\star$	0.01
	$\tilde{E}^\alpha = \tilde{E}^\beta = \tilde{E}$	210
	$\nu^\alpha = \nu^\beta = \nu$	0.3
Isotropic viscoplasticity		
$\tilde{R}_0$	Planar precipitates	0
	Circular precipitates	0.2
	$\tilde{K}$	0.01 – 100
	n	5
Crystal plasticity		
	$\tilde{R}_0^\beta$	0.065
	$\tilde{R}_s^\beta$	$\tilde{Q} = 0.45$, $b=3$
	$\tilde{X}^\beta$	$\tilde{C} = 0.6$, $d=20$
	$\tilde{K}^\beta$	0.1
	n^β	5

$$g = f - \left[h(\phi)\underset{\sim}{\sigma}^{\alpha}\colon \underset{\sim}{\varepsilon}^{\alpha} + \bar{h}(\phi)\underset{\sim}{\sigma}^{\beta}\colon \underset{\sim}{\varepsilon}^{\beta} \right], \tag{93}$$

which is *a priori* not equivalent to (89).

While writing $\langle x \rangle$ the average value, or here the interpolated value, of x according to Eq. (1), the equivalence of (89) and (93) can be also reformulated as follows:

$$\langle \underset{\sim}{\sigma} \rangle \colon \langle \underset{\sim}{\varepsilon} \rangle = \langle \underset{\sim}{\sigma} \colon \underset{\sim}{\varepsilon} \rangle, \tag{94}$$

which is known as the Hill–Mandel principle of macro-homogeneity. In the framework of continuum mechanics, this condition is used to ensure the scale transition. The homogenization schemes to be used within the present framework are required to fulfill this condition.

5. Results

The relevance of the proposed framework is illustrated by investigating the diffusion-controlled growth of misfitted precipitates in supersaturated matrices with different combinations of constitutive laws and different homogenization rules. Two issues will be addressed in particular in this section. (i) First, we critically examine in what respect the different homogenization schemes may impact the kinetics of diffusion-controlled transformations. This constitutes an important point for controlling the outcomes of phase field models applied to transformations at the solid state in order to achieve quantitative predictions. This issue is already critical when only elasticity is involved, and we will first restrict the analysis to this case. (ii) Second, for a specific homogenization scheme, we examine how viscoplasticity impacts the kinetics and the shape evolution of growing precipitates.

For the sake of simplicity, a binary alloy is considered with materials parameters in Table 1. So as to draw general trends relevant for any micrometer-sized microstructures in metallic materials evolving at high temperature, they are reported in their dimensionless forms (denoted with tildes), where the length, time and energy scales are defined respectively by L, commensurate with the system size, the diffusion characteristic time $\tau = L^2/D$ with D the chemical diffusivity of the alloying species, and the ratio $E = \gamma/\delta$ of the interface energy γ to the interface thickness δ. Moreover, the concentrations are scaled by the difference in concentrations $\hat{c}^{\alpha} - \hat{c}^{\beta}$ (Table 1) between the coexisting phases as given by the phase diagram. For the sake of illustration, Norton parameters are recast such as to rescale viscosities K by the energy scale, assuming that the characteristic time entering K is L^2/D (this has no consequence because there is no intrinsic time scale in viscoplasticity Norton type laws). Nonetheless, particular values have been chosen to comply with the growth of oxide layers at the surface of stainless steels (de Rancourt, 2015). In that case, typical physical values of the characteristic scales are L=200 mm, τ = 700 s and $E = 10^9$ J/m^3.

The expression of the mobility of the phase field proposed by Kim et al. (1999) is used to achieve local equilibrium at the interface rapidly, i.e. on times much smaller than the duration of the diffusion-controlled process. $\tilde{M}_{\phi}$ reads:

$$\tilde{M}_{\phi} = \tilde{D}^{\beta}/(6\tilde{\lambda}^2\,\zeta), \tag{95}$$

with

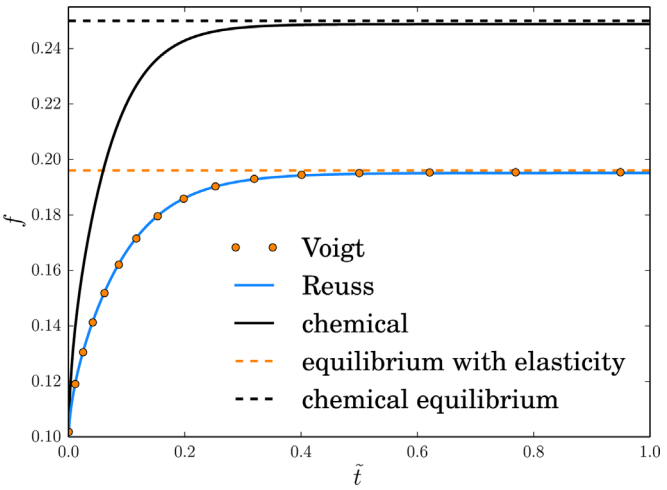

Fig. 1. Growth kinetics of planar precipitates in an initially supersaturated matrix driven by the diffusion of the alloying species, without elasticity (black) and with elasticity (blue and orange). The corresponding equilibrium fractions are indicated with horizontal dashed lines. (For interpretation of the references to color in this figure caption, the reader is referred to the web version of this paper.)

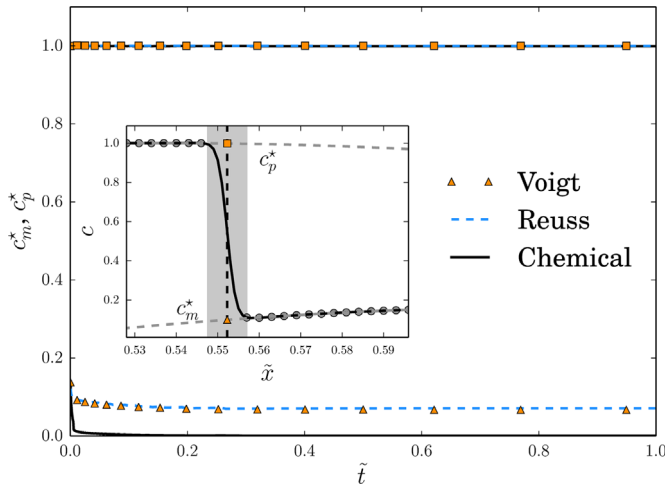

Fig. 2. Evolution of the concentrations at the interface (squares: matrix; triangles: precipitate) during growth, retrieved from the successive concentration fields by extrapolation from the bulk into the diffuse interface at the level set $\phi = 0.5$ (inset). (For interpretation of the references to color in this figure caption, the reader is referred to the web version of this paper.)

$$\zeta = \tilde{k}^\alpha \tilde{k}^\beta (\hat{c}^\alpha - \hat{c}^\beta)^2 \int_0^1 \frac{h\bar{h}}{\bar{h}\tilde{k}^\alpha + h\tilde{k}^\beta} \frac{d\phi}{\phi(1-\phi)}.$$

In all the subsequent calculations, the initial microstructure is set such that the phase field features an equilibrium profile in tanh in the direction normal to the interface. The initial concentration field c is defined such as to display the chemical equilibrium value in the precipitate, i.e. $c^\alpha = \hat{c}^\alpha$, and a supersaturated constant value in the matrix, i.e. $c^\beta > \hat{c}^\beta$, sufficient to promote growth. The following boundary conditions have been considered in all the calculations: $\nabla c \cdot \vec{n} = 0$ and $\nabla\phi \cdot \vec{n} = 0$, where $\vec{n}$ denotes the outward normal vectors; beside plane strain conditions, zero average in-plane stresses are enforced by constraining the boundaries to remain flat without resulting forces.

The influence of the mesh size and time step has been systematically investigated for all 1D simulations to ensure that the results are fully converged with respect to the discretization of the partial differential equations. An automatic time step has been used ensuring that relative variations between two successive steps remain below upper bounds minimizing the error associated with time integration. The convergence of all 1D cases with respect to space discretization has been sys-

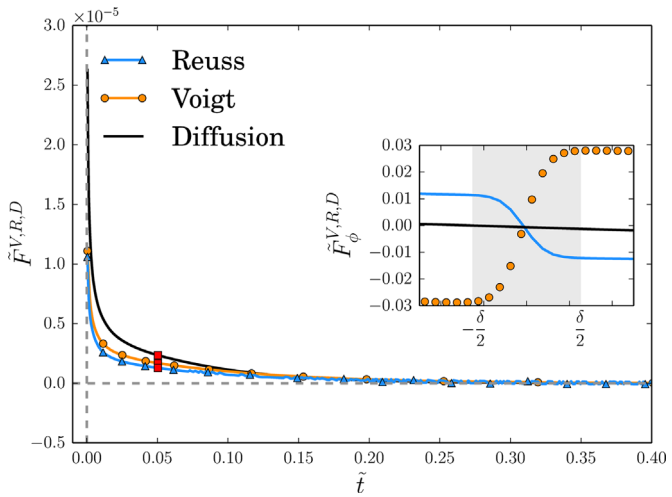

Fig. 3. Evolution of the driving force for interface motion obtained by integrating the profiles of $\tilde{F}_\phi$ (snapshot at $\tilde{t} = 0.5$ in the inset) according to Eq. (96): without elasticity (black), Voigt (orange) and Reuss (blue). (For interpretation of the references to color in this figure caption, the reader is referred to the web version of this paper.)

tematically checked by performing series of calculations with increasing numbers of linear elements. As usual, the lower bound is set by the number of elements within the diffuse interface: 10 linear elements have been found to be sufficient to resolve the interface and prevent grid pinning. The total number of elements is then set by the ratio of the total size over the interface thickness. In our calculations, the number of elements typically ranges from 500 to 2000. The 2D simulations have been performed without systematic mesh refinement but the grid and time steps have been wisely selected with respect to (i) the observations made from the 1D simulations, and (ii) simple test cases that can be compared with analytical predictions (e.g. the spherical growth worked out in Ammar et al., 2011).

5.1. Influence of the homogenization scheme on diffusion-controlled growth kinetics

First, the influence of the homogenization scheme on the growth kinetics is investigated in the purely elastic case with respect to the purely chemical case.

For that purpose, a simple planar precipitate of width $L/10$ in a 1D system is first considered, with length L ($f^0 = 0.1$). The matrix is initially supersaturated in the alloying species with concentration $c^0 = 0.055 > \hat{c}^\beta$ so as to promote the growth of the precipitate. Indeed, this concentration corresponds to precipitate fractions $f=0.25$ and $f=0.197$ without and with elasticity respectively, as predicted by the minimization of the free energy of the equivalent sharp interface system, e.g. Cahn and Larché (1984) and Ammar et al. (2009b). These values are reported in Fig. 1 with the dashed horizontal lines, along with the kinetic curves of the corresponding growth processes. All the kinetics follow $\sqrt{t}$ laws as expected for diffusion-controlled processes, during a first stage ($\tilde{t} < 0.1$) before saturation at the relevant equilibrium phase fractions. These kinetics are consistent with interfaces reaching rapidly local equilibrium after a short initial transient due to the finite phase field mobility as shown in Fig. 2, where the interface concentrations have been retrieved by extrapolation of the profiles in the bulk regions abutting the diffuse interface up to the level set $\phi = 0.5$ (inset of Fig. 2). It is worth stressing that both Voigt (orange) and Reuss (blue) homogenization schemes give the same interface concentrations and consequently the same kinetics. The slower kinetics observed with elasticity can be attributed to the impact of elasticity on the interface concentrations as clearly shown in Fig. 2, in agreement with the predictions of the corresponding sharp interface conditions, e.g. Johnson and Voorhees (1999), similarly to recent results reported in Ammar et al. (2011). Indeed, the concentration gradient in the matrix at the interface which drives the precipitate growth according to the interface solute balance is less pronounced than without elasticity. It can also be noted that the concentration in the matrix for the elastic case exhibits a slow variation during the growth process: this is due to the evolution of stress and strain at the interface impacting the equilibrium concentrations more significantly in the matrix because of the moderate curvature $\tilde{k}^\beta$ (Table 1).

It is observed that, quite unexpectedly, Voigt and Reuss schemes give very close results. Indeed, as shown in Mosler et al. (2014) and Durga et al. (2013), both schemes display different elastic energy density profiles within the interface which could lead to different interface conditions and kinetics at first sight. This was suggested in Mosler et al. (2014) where $\tilde{F}_\phi$ is called a driving force. However, $\tilde{F}_\phi$ is not the relevant quantity to inspect for the interface motion, but rather its integral counterpart $\tilde{F}$ given by, e.g. Perevoshchikova (2012):

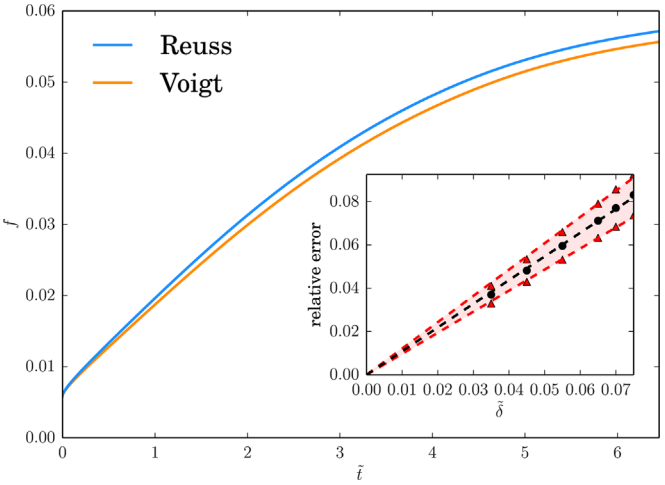

Fig. 4. Growth kinetics of circular precipitates in an initially supersaturated matrix, predicted with Reuss (blue) and Voigt (orange) schemes, with $\tilde{\delta}$ = [0.035, 0.045, 0.055, 0.065, 0.07, 0.075]. Inset: average relative difference between both kinetics vs. interface thickness. (For interpretation of the references to color in this figure caption, the reader is referred to the web version of this paper.)

$$\tilde{F} = \int_{-\tilde{\delta}/2}^{\tilde{\delta}/2} \tilde{F}_\phi \, h' \, \frac{\partial \phi}{\partial x} dx, \tag{96}$$

which should vanish if the interface is exactly at local equilibrium. Thus, the evolution of $\tilde{F}$ is plotted in Fig. 3 using the profiles of $\tilde{F}_\phi$ at each time step, as illustrated in the inset of Fig. 3. In all cases, a sharp drop is observed at the very beginning from the initial values corresponding to initial out-of-equilibrium conditions, down to small values corresponding to interfaces close to local equilibrium. The non-zero values observed during the growth process can be attributed to some residual interface friction (Hillert, 1999; Perevoshchikova et al., 2014). Indeed, as shown in Perevoshchikova (2012) with a rigorous second-order asymptotics analysis of the model in the pure chemical case, the following relationship holds between the driving force and the phase field mobility $\tilde{M}_\phi$ provided that the profile of chemical potential μ in the precipitate is flat:

$$\tilde{F}^\alpha = \frac{\tilde{v}}{6}\left(\frac{1}{\tilde{\lambda}\tilde{M}_\phi} - \frac{\zeta}{\tilde{D}}\right), \tag{97}$$

with $\tilde{v}$ being the interface velocity, and where the second term on the right hand side is associated with dissipation by trans-interface diffusion (Hillert, 1999). It must be emphasized that the driving force is evaluated on the precipitate side of the interface, because it displays a gradient within the diffuse interface when the alloying species mobility $\tilde{M}$ (and $\tilde{D}$) depends on ϕ. In the particular case of constant $\tilde{D}$, it can be shown that the driving force is constant over the interface up to first order in $\tilde{\lambda}$ (Karma and Rappel, 1998) so that the driving force can be related to the interface friction directly, i.e. $\tilde{F}^\alpha = \tilde{F} = \tilde{v}/\tilde{M}$. Then, the interface friction can be cancelled by a proper choice of the phase field mobility as proposed by Kim et al. (1999) (Eq. (95)). However, due to the difference in diffusivities of about two order of magnitudes in the present calculations (Table 1), there remains some residual interface friction linear in $\tilde{v}$ and scaling with $\tilde{\lambda}$. With elasticity, even if $\tilde{F}_\phi$ features very different profiles for the Voigt and Reuss schemes as shown in the inset of Fig. 3, the corresponding driving forces $\tilde{F}$ are nearly the same, in agreement with the formal difference $\tilde{F}_\phi^V - \tilde{F}_\phi^R$ that vanishes like $\tilde{\lambda}$ (de Rancourt, 2015). This explains the very good agreement between both schemes in terms of interface conditions and kinetics in the planar case. It can be noted that because elasticity slows down the growth process, the interface friction is lower than in the chemical case, but remains of the same order.

To complete the comparison between the Voigt and Reuss homogenization schemes, we have considered the case of a circular precipitate growing in a supersaturated matrix. Indeed, in this case, two additional contributions due to the interface curvature can modify the interface conditions and consequently the growth kinetics. First, the interface energy changes the equilibrium concentrations through the Gibbs–Thomson relationship. Second, excess stress and strain can also be involved in the interface conditions (Johnson and Alexander, 1986). In Fig. 4, the evolution of the precipitate fraction is plotted for the Voigt and Reuss schemes. Contrary to the planar case, Reuss gives a growth process slightly faster than Voigt, with a difference in phase fraction of at most 0.2%. When decreasing the interface thickness, both schemes converge toward the same evolution in between the blue and orange curves. As shown in the inset of Fig. 4, the maximal relative difference between Reuss and Voigt scales linearly with the interface thickness and vanishes for a sharp interface, as inferred from the extrapolation of several calculations down to $\tilde{\delta} = 0$. This is in agreement with a second-order asymptotics analysis of a

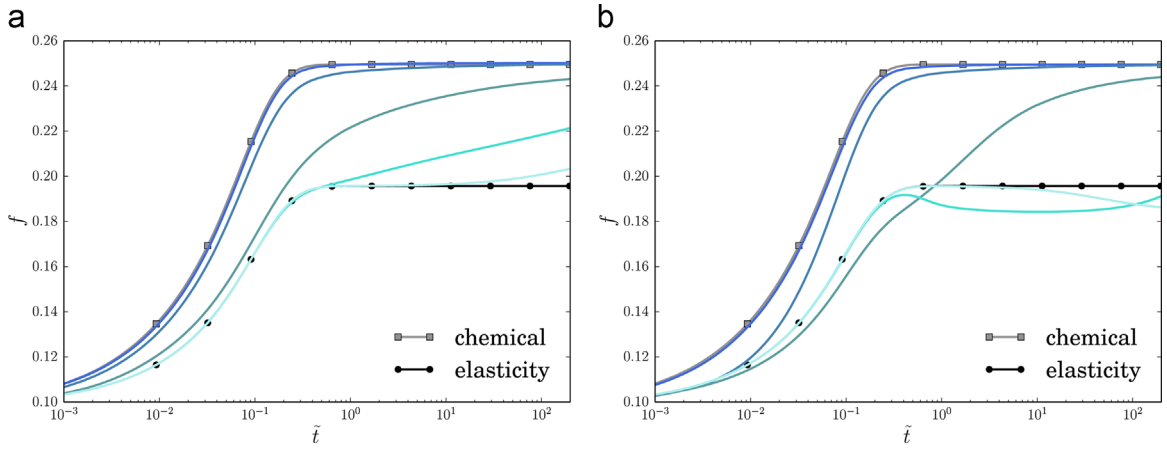

Fig. 5. Growth kinetics of planar precipitates in an initially supersaturated matrix driven by the diffusion of the alloying species, without elasticity (squares), with elasticity (dots), and with viscoplastic relaxation (left) in the precipitate, or (right) in the matrix, for different viscosities $\tilde{K} \in [0.1, 1, 5, 18, 50]$ (from dark blue to turquoise). (For interpretation of the references to color in this figure caption, the reader is referred to the web version of this paper.)

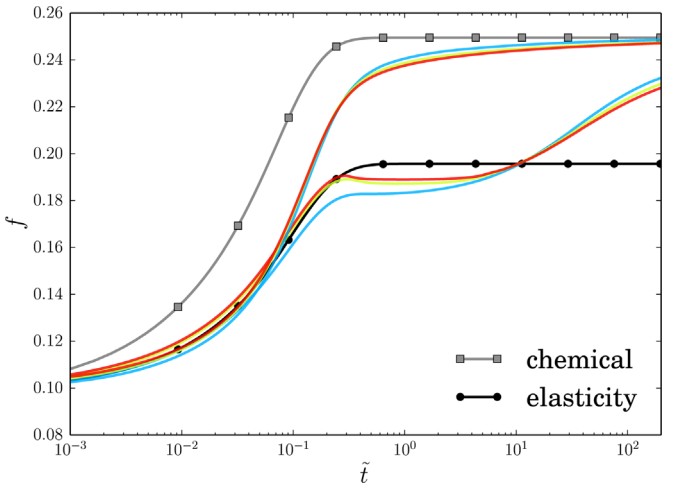

Fig. 6. Growth kinetics of planar precipitates in an initially supersaturated matrix driven by the diffusion of the alloying species, without elasticity (squares), with elasticity (dots), and with viscoplastic relaxation in the matrix for $\tilde{K} = 9$ (upper set) and $\tilde{K} = 2$ (lower set) and different interface thicknesses $\tilde{\delta}$: 0.005 (red), 0.01 (green) and 0.025 (blue). (For interpretation of the references to color in this figure caption, the reader is referred to the web version of this paper.)

particular phase field model with elasticity where the deviations from the sharp interface conditions scale linearly with the interface thickness and involve contributions that are linear in the interface curvature (Appolaire and Le Bouar, 2015).

It can be concluded that the interface conditions delivered by both homogenization schemes are close to each other in agreement with the corresponding sharp interface conditions in the elastic case. If there is no formal proof that this good match would be preserved when viscoplasticity is involved, we have nonetheless used only Voigt scheme in the following investigations for the sake of clarity.

5.2. *Influence of viscoplasticity on diffusion-controlled growth kinetics*

Next, calculations involving viscoplasticity are performed so as to assess its possible impact on the kinetics of diffusion-controlled transformations. By comparing to purely chemical and elastic kinetics, we will address an issue which has long been ignored due to the lack of modeling approach encompassing both phase transformations and plasticity: in what respect invoking plastic relaxation at high temperature is sufficient to discard any influence of mechanics on the kinetics of

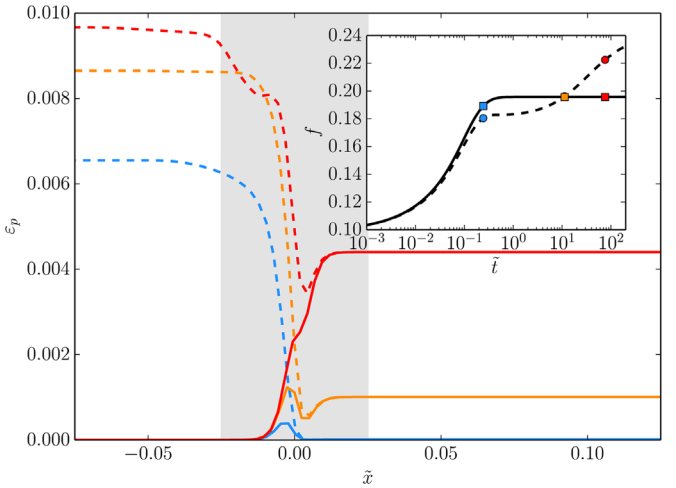

Fig. 7. Profiles of the plastic strain ε_p^m (dashed line) and ε_p (continuous line) across the diffuse interface (location x_0) at different times (0.2, 11 and 75). Inset: growth kinetics for the elastic (continuous line) and viscoplastic ($\tilde{K} = 9$, dashed line) cases. (For interpretation of the references to color in this figure caption, the reader is referred to the web version of this paper.)

diffusion-controlled transformations. Moreover, we will take advantage from investigating simple cases to put into evidence subtle effects related to viscoplasticity in diffuse interfaces. For that purpose, a simple Norton constitutive law is considered in either α or β phase with parameters in Table 1. It is assumed that all phases are initially elastic, i.e. $\underset{\sim}{\varepsilon}^p(x) = 0,\ \forall\, x$. Moreover, it is worth mentioning that within the present framework, the growing phase does not inherit plasticity from the mother phase, as discussed by Ammar et al. (2014).

First, the growth of a planar viscoplastic precipitate in an elastic matrix is studied. The growth kinetics are plotted in Fig. 5a with a semi-log scale for different $\tilde{K}$ ranging from 0.1 to 500. They all nearly lie in between the chemical and elastic kinetics, investigated in the previous section. For large $\tilde{K} \geq 500$, the kinetics follows the elastic kinetics. Once the elastic equilibrium fraction is reached, viscoplastic relaxation induces a slow increase of the precipitate fraction up to the chemical equilibrium fraction. A quick inspection of the concentration fields (not shown) indicates that, at this stage, the concentrations are homogeneous in both phases and evolve according to the interface conditions which are modified by the plastic strain.

When $\tilde{K} \lessapprox 5$, deviation from the elastic case is observed from the very beginning of the growth process, indicating that the viscoplasticity relaxation is as fast as the chemical diffusion driving the growth process. For $\tilde{K} \lessapprox 0.1$, the kinetics reaches the chemical growth kinetics indicating that the viscous effects are negligible and that the plastic relaxation is instantaneous: this is the regime usually assumed in the diffusion-controlled models used to predict kinetic diagrams of alloys, e.g. Appolaire et al. (2005). The present results clearly show that if this assumption is likely to be valid for slow transformations in conditions close to equilibrium, it can be questioned for faster transformations where kinetics may be slower than predicted by conventional model discarding mechanical effects. Moreover, it must be kept in mind that for more complex morphologies, viscoplasticity may not relax entirely the misfit generated stresses such that the chemical case cannot constitute the limit case, as shown recently in Cottura et al. (2015).

The opposite case has also been investigated: the growing precipitate remains elastic whereas the matrix is viscoplastic (Fig. 5b). As in the previous case, the stresses relax very rapidly for $\tilde{K} < 0.1$ and the kinetics follows the chemical case. When increasing the viscosity of the matrix above 5, the growth kinetics starts to follow the elastic kinetics but becomes surprisingly slower than the elastic kinetics at some point: the greater the value of $\tilde{K}$ the later this feature is observed. For $\tilde{K}$ above ≈10, this feature is observed after that the elastic equilibrium phase fraction has been reached. Then f decreases below the elastic equilibrium fraction f=0.197 down to $f \approx 0.183$, a value common to all $\tilde{K} \gtrapprox 10$. Finally, f increases slowly towards the chemical equilibrium fraction on a time scale set by the viscoplastic relaxation, as for the viscoplastic precipitates in an elastic matrix. Actually, the incursions below the limiting curve for pure elasticity are spurious effects due to the diffuse interface, as shown in Fig. 6 where the same calculations have been performed with different thicknesses, $\tilde{\delta} = 5{\cdot}10^{-3},\ 10^{-2}$ and $2.5{\cdot}10^{-2}$. Indeed, for a viscous matrix with large $\tilde{K}$ (>5) featuring a decrease below the elastic equilibrium fraction, decreasing the interface thickness has a strong impact on the amplitude of the drop. Fortunately, for smaller viscosities, $\tilde{K} \leq 2$, associated with characteristic times for viscoplastic relaxation shorter than the growth duration, the influence of the interface thickness remains negligible. To understand further the origin of this spurious effect, we have inspected the evolutions of the profiles of F_ϕ (not shown) between the elastic case and the viscoplastic case with $\tilde{K} = 9$: very early in the growth process, the elastic contribution to F_ϕ is relaxed within the interface on the precipitate side. This relaxation can be attributed to the increase in the cumulative plastic strain localized in the diffuse interface on the precipitate side, as shown in Fig. 7.

Initially, the von Mises equivalent stress is much larger in the precipitate than in the matrix because the initial fraction of

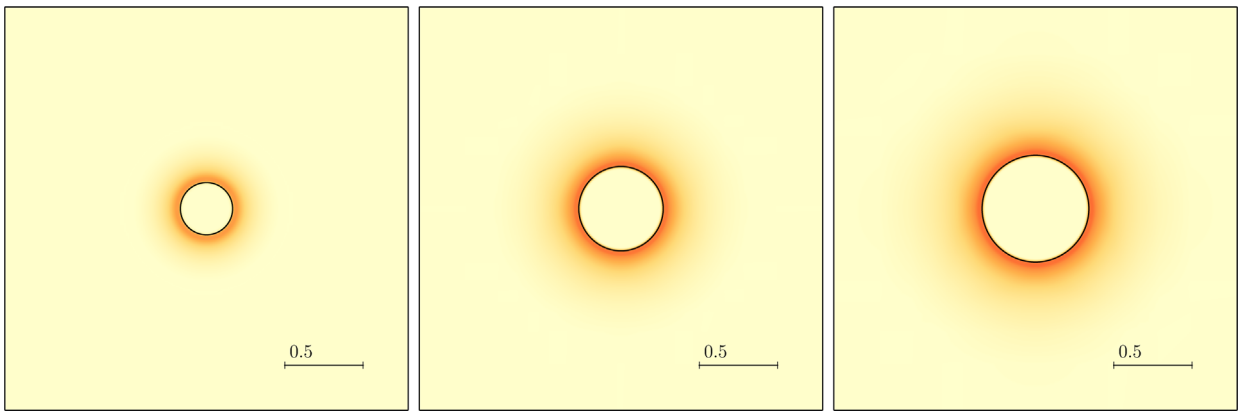

Fig. 8. Snapshots (enlargements of the 4 × 4 system) of the cumulative equivalent plastic strain (red maximum value=0.01) at times ($1.3e^{-6}$, 0.5 and 1.1) during the diffusion-controlled growth an elastic precipitate in a supersaturated matrix with isotropic viscoplastic behavior. (For interpretation of the references to color in this figure caption, the reader is referred to the web version of this paper.)

precipitate is small. It is important to recall that, within any phase field framework relying on homogenization, the constitutive laws of a given phase operate in the whole system and not only where this phase is present, as shown in Fig. 7 (dashed lines). Thus, the viscoplastic relaxation associated with the matrix proceeds in the precipitate first. In the simple case of homogeneous elasticity, the homogenized plastic strain $\underset{\sim}{\varepsilon}_p$ simply amounts to $\bar{h}(\phi)\underset{\sim}{\varepsilon}_p^{\beta}$: the weighting by $\bar{h}(\phi)$ localizes $\underset{\sim}{\varepsilon}_p$ in the diffuse interface on the precipitate side (continuous line in Fig. 7). Then, the peak of plastic strain in the interface rises faster than the plastic strain in the matrix due to the difference in von Mises stresses (blue and orange curves): this changes the driving force and slows down the growth kinetics with respect to the pure elastic case. At longer times, viscoplasticity proceeds also in the matrix and the peak in the interface is overcome, when the kinetics progressively reaches the chemical curve (red curve). When the matrix displays less viscosity effects, this spurious effect remains minor because the relaxation in the matrix occurs very early and prevents the peak to be prominent during the transformation. In the alternative case where the precipitate undergoes viscoplastic relaxation whereas the matrix remains elastic, the same spurious kinetic effect is likely to be observed in general. But in the present calculations, the fraction of matrix remains much larger than the fraction of precipitate during the whole growth. Consequently, the von Mises stress remains lower in the matrix than in the precipitate: viscoplastic relaxation proceeds faster in the precipitate, and the spurious peak is overcome at the very beginning of growth.

These calculations demonstrate that the coupling of nonlinear constitutive laws with a diffuse interface approach is more involved than the equivalent homogenization rules in phase field models without mechanics, e.g Kim et al. (1999). Hence, it seems mandatory to critically analyze any such coupling in simple and well-known situations, as carried out in the present study. Moreover, it must be emphasized that it is currently not clear if the kind of spurious effects discussed above plagues only homogenization schemes. Fortunately, from a pragmatic point of view, we have shown that these spurious effects can be kept within reasonable bounds provided that the viscosity is moderate, such that the time scale for viscoplastic relaxation is comparable to or smaller than the time scale for diffusion (in particular for time independent plasticity as implemented in Ammar et al., 2009b, 2011).

It is also worth mentioning that the spurious effect can be suppressed by imposing *ad hoc* conditions on the rates of internal variables, e.g.

$$\begin{cases} \dot{\varepsilon}_p^{\alpha} = 0 \quad \text{where } \phi > \phi^{+} \\ \dot{\varepsilon}_p^{\beta} = 0 \quad \text{where } \phi < \phi^{-} \end{cases} \tag{98}$$

Preliminary calculations have shown that such a scheme can cure the spurious problems although its theoretical foundations remain to be settled rigorously and deserve more extensive investigations deferred to future investigations.

5.3. *Influence of viscoplasticity on growth shapes*

Finally, the interplay between viscoplasticity and morphological evolutions during the diffusion-controlled growth of precipitates is investigated. In contrast with recent works addressing issues concerning specific materials and involving complex situations, such as rafting in Ni-base superalloys (Gaubert et al., 2010; Cottura et al., 2012) or Widmanstätten plate growth (Cottura et al., 2015), we focus on a simple generic situation by examining the destabilization of a circular precipitate growing in a supersaturated matrix, which is known to undergo a Mullins–Sekerka morphological destabilization (Mullins

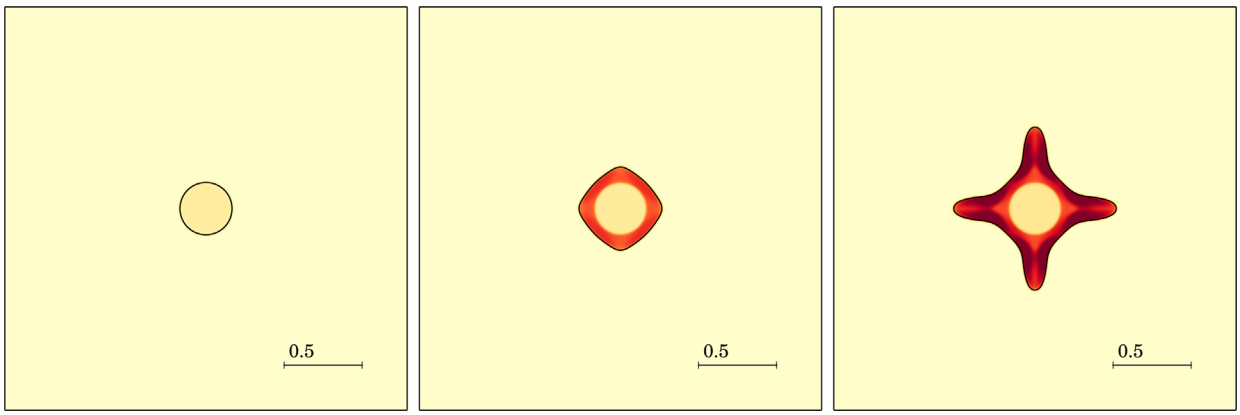

Fig. 9. Snapshots (enlargements of the 4×4 system) of the cumulative equivalent plastic strain (red maximum value$=$0.03) at times ($1.3e^{-6}$, 0.5 and 1.1) during the diffusion-controlled growth a precipitate with isotropic viscoplastic behavior in an elastic supersaturated matrix. (For interpretation of the references to color in this figure caption, the reader is referred to the web version of this paper.)

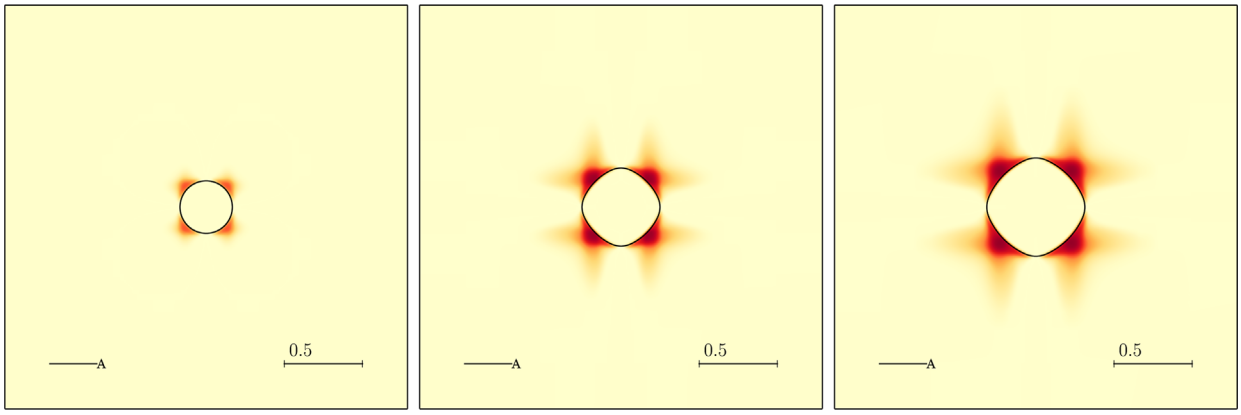

Fig. 10. Snapshots (enlargements of the 4×4 system) of the cumulative equivalent plastic strain (red maximum value = 0.02) at times ($2.8e^{-4}$, 0.6 and 1.3) during the diffusion-controlled growth an elastic precipitate in a supersaturated matrix with anisotropic viscoplastic behavior (slip system denoted by A). (For interpretation of the references to color in this figure caption, the reader is referred to the web version of this paper.)

and Sekerka, 1963). It has been shown in Leo and Sekerka (1989) that elasticity may change the critical radius for destabilization, depending on the ratio of shear moduli between the precipitate and the matrix: the destabilization of a hard precipitate growing inside a soft matrix is delayed whereas the inverse situation is predicted for a soft precipitate in a hard matrix.

Using the conclusions of the previous section, only moderate viscosities are considered to avoid the spurious effects associated with the diffuse interface. Moreover, contrary to the previous calculations, a yield stress $\tilde{R}_0 = 0.2$ is chosen in the viscoplastic flow rules so as to comply with the parameters used in the crystal plasticity model (Table 1). Circular misfitting precipitates of radius $\tilde{r}_0 = 0.15$ are located at the center of a 4×4 square matrix supersaturated with $c^0 = 0.05$ so as to promote growth. Different combinations of constitutive laws are considered: (i) an elastic precipitate embedded in a matrix with isotropic viscoplasticity; (ii) a precipitate with isotropic viscoplasticity embedded in an elastic matrix; and (iii) an elastic precipitate embedded in a matrix endowed with crystal plasticity behavior.

The evolution of the precipitate in the first case is shown in Fig. 8 where the cumulative plastic strain ranges from 0 (light yellow) to 2% (orange). The precipitate remains circular for the whole growth duration. The plastic strain is localized around the precipitate in the matrix and is not inherited by the precipitate. Its maximum value, located at the interface, remains constant, and the radius of the plastic zone increases with the precipitate radius in agreement with the analytical solution and phase field calculations considering time independent plasticity (Ammar et al., 2011).

In the second case (Fig. 9), the viscoplastic precipitate growing in an elastic matrix undergoes a very different evolution: the circular shape is rapidly destabilized to give rise to a star shape with four branches aligned with the discretization grid. A shell of plastic strain develops inside the precipitate close to the interface very early during the growth process. During the transient stage of destabilization, the increase in plastic strain is slightly lower along the directions of destabilization (lighter regions in Fig. 9) than in other directions. But rapidly the tips grow at a constant rate along the horizontal and vertical directions. This is very similar to dendrite growth, observed also at the solid state in alloys with moderate isotropic misfits partially relaxed by misfit dislocations at the interface, e.g. Husain et al. (1999), mimicked crudely by viscoplasticity in the present work, see also Appolaire et al. (2010). Note that the unstable modes are selected by the slight anisotropy of interface energy induced by the discretization grid, e.g. Bösch et al. (1995): indeed, by twisting the square mesh with respect to the horizontal axis, we have obtained star shaped precipitates with branches no longer aligned horizontally and vertically but aligned with the mesh (not shown).

The differences between both cases are similar to the differences found by Leo and Sekerka (1989) in the pure elastic case between hard precipitate in soft matrix and soft precipitate in hard matrix. Indeed, qualitatively, viscoplastic relaxation by a J_2 theory amounts qualitatively to decrease the secant shear modulus, above the yield stress. Then, an elastic precipitate in a viscoplastic matrix behaves similarly to a hard precipitate in a soft matrix and displays a larger critical radius for morphological destabilization, whereas a viscoplastic circular precipitate behaves like a soft precipitate in an elastic matrix and destabilizes at a smaller radius. This interpretation is supported by additional calculations, not shown, where strain-hardening is introduced in the viscoplastic precipitate, and where the destabilization occurs later than without hardening.

Finally, the growth of an elastic precipitate is computed for a matrix that displays anisotropic viscoplasticity along a single slip system (indicated by letter A in Fig. 10). Very early in the growth process, plastic strain is localized near the interface in the matrix at 45 with respect to the square box with short horizontal and vertical bands respectively aligned and perpendicular to the slip direction (slip and kink bands). The resolved shear stress is maximal at this angle around a circular precipitate with isotropic misfit, e.g. Geslin et al. (2014). The heterogeneous distribution caused by the anisotropy of plastic

relaxation induces an anisotropic shape evolution with smooth corners developing along the horizontal and vertical directions, where there is no plastic relaxation. This case demonstrates that the symmetries of plastic relaxation can interfere with the other symmetries that drive the morphology of the microstructures, as already shown in phase field calculations of rafting in Ni-based superalloys (Gaubert et al., 2010; Cottura et al., 2012). Moreover, it demonstrates that the interplay of plasticity and diffusion-controlled phase transformations cannot be predicted with simple qualitative arguments: whereas plasticity promotes growth of a planar interface with respect to elasticity as shown in Section 5.2, it can hinder growth as in Fig. 10. This complexity which discards any oversimplified arguments based on overall balances, e.g. Embury et al. (2003), can be related to the indirect influence of mechanics on the morphologies through the boundary conditions of diffusion driving the evolution processes.

6. Conclusions

A general framework has been established describing diffusion driven phase transformation in elastoviscoplastic multicomponent materials. It is based on the combination of homogenization and phase field approaches. In contrast to existing frameworks applied to nonlinear materials, mainly relying on parameter interpolation, it has the advantage that arbitrary types of material behavior for the different phases can be combined within a consistent thermomechanical theory. The exploitation of the second law of thermodynamics has been used to motivate two privileged homogenization schemes, namely the Voigt/Taylor and Reuss/Sachs models, respectively obtained from the consideration of the Helmholtz or Gibbs free energy density potentials. It extends the strategy initiated by Kim et al. (1999) and limited to the diffusion part of the model, to the case of nonlinear mechanical behavior of the phases. The thermodynamic consistency of the model ensuring the positivity of the dissipation rate at each time and each material point was established for a large class of material behavior, so-called standard generalized materials.

The computational analysis of the model lead to the following main results.

- Voigt and Reuss schemes lead to the same diffusion-controlled growth kinetics of an elastic precipitate within an elastic matrix at the asymptotic limit of vanishingly small width of the diffuse interface.
- The competition between the characteristic times for chemical diffusion of species and viscoplastic stress relaxation leads to complex kinetic behaviors compared to the purely chemical and elastic reference cases.
- Viscoplasticity has been shown to play a significant role in the shape bifurcations undergone by growing circular precipitates, controlling the onset of the Mullins–Sekerka instability.
- Crystal plasticity of the matrix was shown to induce anisotropic growth of the precipitate due to the formation of slip and kink bands at preferred locations of interfaces.

Even though homogenization phase field models should be designed in such a way that they provide the same sharp interface asymptotic response, the choice of a specific homogenization scheme in the proposed theory can have a significant impact on the material response in the following cases. First, in the case of a structured diffuse interface, the homogenization scheme should take the morphology of the interface into account (case of a laminate for example). Secondly, some schemes can exhibit a computational advantage, like improved convergence of an implicit numerical scheme. It is the case of the Voigt scheme for the implicit finite element method used in the present work in conjunction with a Runge–Kutta method. Finally, if the phase field model is intended for application at a mesoscopic scale, like that of a polycrystal, so that thick interfaces are required for computational efficiency, then it is anticipated that the specific choice of the homogenization scheme will have a non-negligible effect on kinetics and morphology of phases.

Current applications of the presented theory are dedicated to the modeling of oxide growth in the bulk and in the grain boundaries of polycrystals. The question of inheritance of plasticity and hardening should also be considered within a homogenization based phase field approach, as initiated in Ammar et al. (2014). This should however be supported by relevant experimental data including field measurements of concentration, strain and crystal orientation.

Acknowledgments

The authors thank Dr. T. Couvant for fruitful discussions during the development and application of the model. SF and VdR also thank Dr. E.P. Busso for fruitful discussions. Funding by Chaire EDF at Mines ParisTech for the PhD work of the first author is gratefully acknowledged.

Appendix A. Finite element implementation

The time evolution of the multiphysical free boundary problem is based on a first-order finite difference time discretization within a finite element space discretization. The developed elements embed several degrees of freedom, represented by scalar and vector fields, that represent quantities of different physical nature. The evolution of such fields is

then computed from the constitutive laws obtained in the previous sections, which define the behavior of the material of interest. At each time step, equilibrium is found by means of an implicit Newton algorithm whereas the evolution of internal variables is calculated with an explicit Runge–Kutta algorithm of second order with automatic time stepping.

The natural choice of degrees of freedom regarding finite-element modeling is:

$$\text{DOF} = \{\phi,\ c_i,\ \underline{\boldsymbol{u}}\}, \tag{A.1}$$

but this set is not sufficient to compute all the state laws because c_i^α and c_i^β must be explicitly evaluated. Because (36) connects c_i^α and c_i^β together, so that c_i^α is then sufficient to evaluate c_i, see (1), an appropriate set of degrees of freedom is:

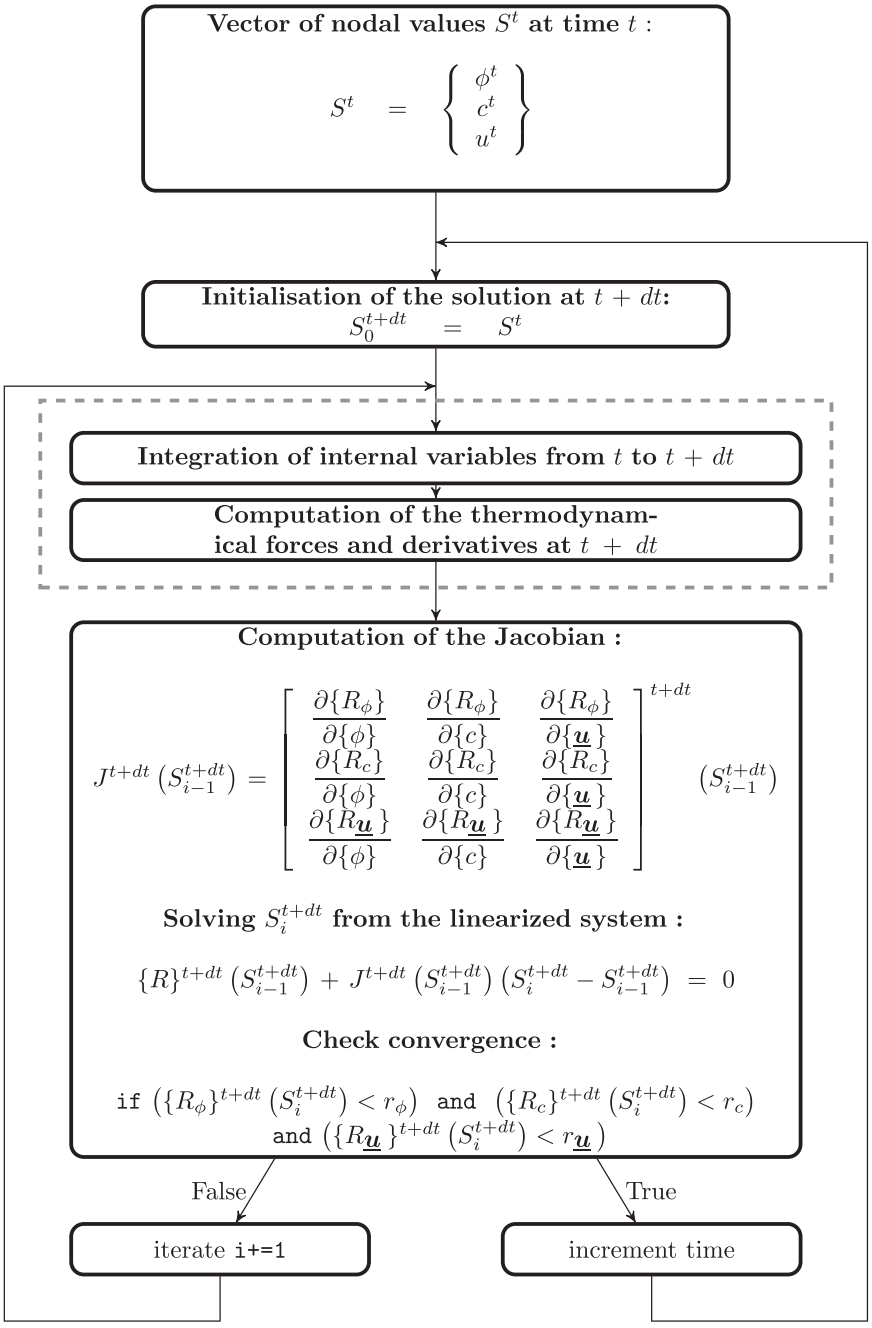

Fig. A1. The Newton algorithm is illustrated in the form of a flow chart for the case of a multiphysical problem containing a phase field ϕ, one or several concentration fields c and displacements $\underline{\boldsymbol{u}}$. The steps located within the dashed gray box call the material behavior, where integrated variables, thermodynamic forces along with their derivatives are evaluated at $t + dt$. Two sets of constitutive laws can be considered that are dependent on the chosen homogenization scheme, either Voigt and Reuss.

$$\text{DOF} = \{\phi,\ c_i^{\alpha},\ \underline{\boldsymbol{u}}\}, \tag{A.2}$$

A.1. Monolithic global resolution of the coupled problem

The time evolution of the multiphysical set of nodal variables is obtained by solving the weak form of the balance equations (9) and (10), by nullifying their residuals R, defined as the difference between the left and right-hand side of the weak form of the balance equations, using the Newton algorithm illustrated in Fig. A1.

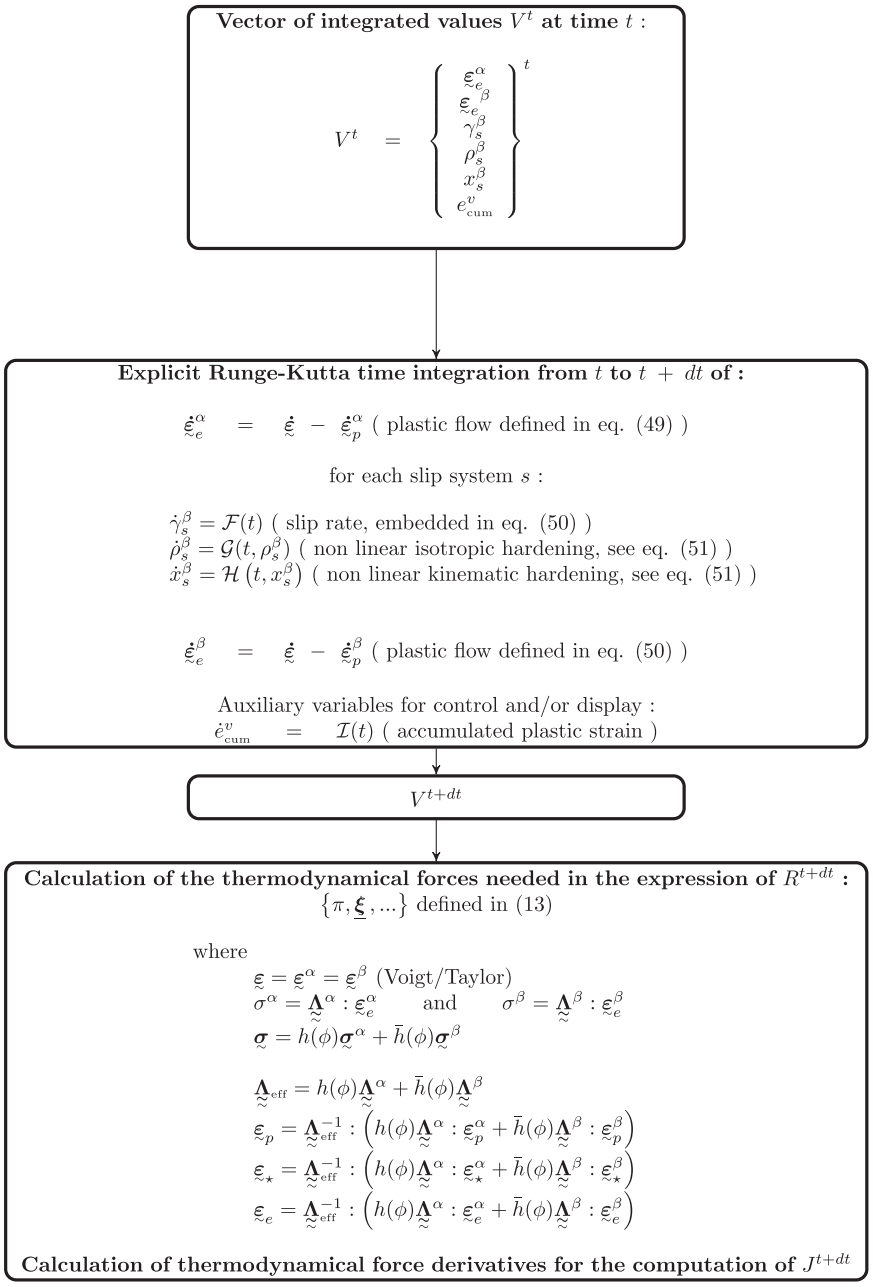

Fig. A2. Algorithm used in the computation of time integrated variables, thermodynamic forces and derivatives in the case of the Voigt/Taylor approach. Integrated variables can be used for the control of the global time stepping, e.g. $\int_t^{t+dt} \dot{e}_{\text{cum}}^{v}$ must not exceed a given increment for any dt.

A.2. Local integration of the constitutive equations according to Voigt homogenization scheme

See Fig. A2.

A.3. Local integration of the constitutive equations according to Reuss homogenization scheme

See Fig. A3.

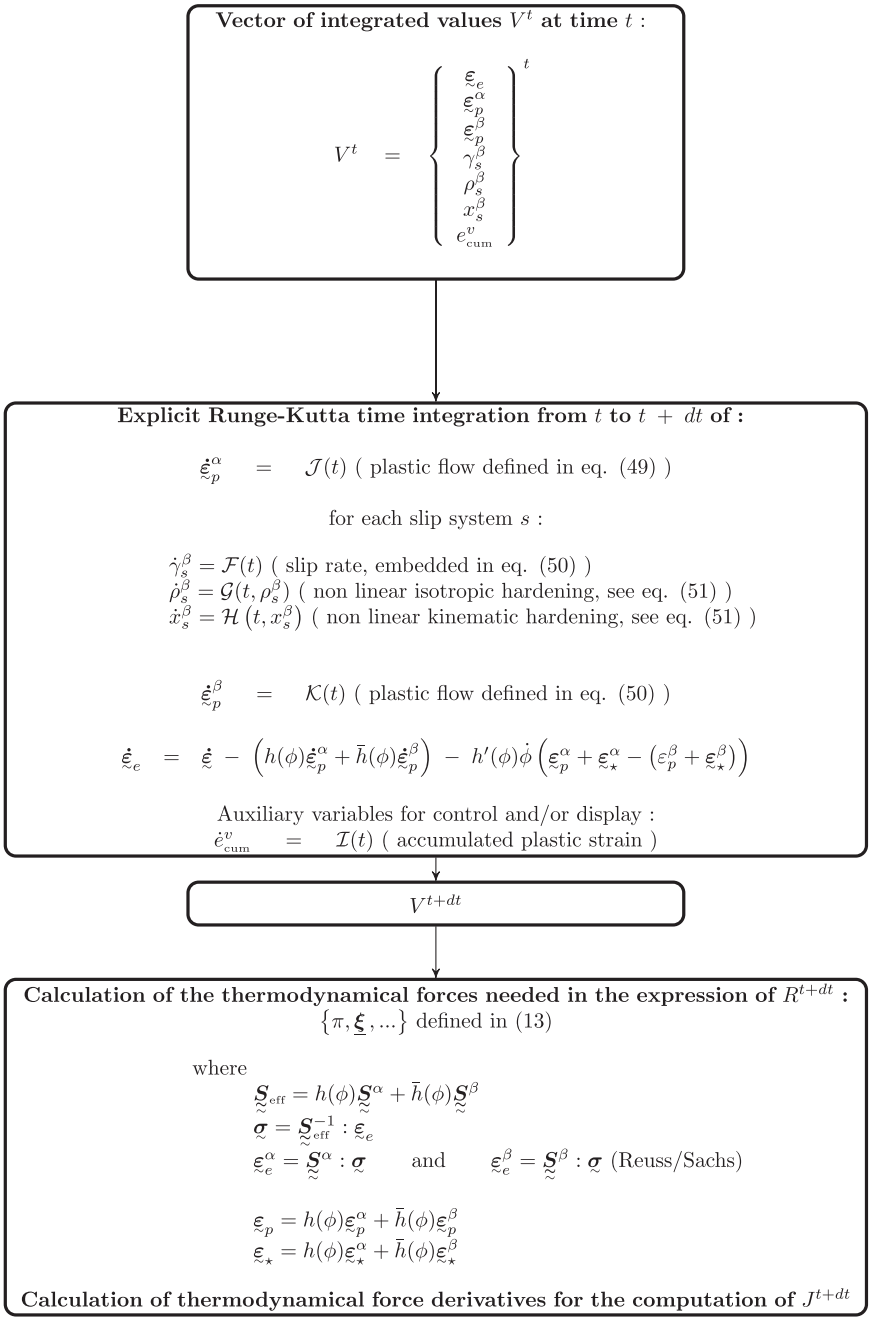

Fig. A3. Algorithm used in the computation of time integrated variables, thermodynamic forces and derivatives in the case of the Reuss/Sachs approach. The integration of the elastic strain involves external fields such as the order parameter and its derivative, which is known to reduce the accuracy of the Runge–Kutta scheme.

Appendix B. Finite element discretization

The numerical approach for the three dimensional finite element modeling of the multiphysical problem is here developed by first choosing finite elements based on n nodes, each endowed with several degrees of freedom, that can be either scalar or vector valued. A Gauss integration procedure is performed where integration point values are obtained from the product of shape functions matrices N, for scalar nodal values and $\mathbf{N}$ for vector nodal values, with the nodal values. Gradients can be computed from the product of the gradient operator $\mathbf{B}$, for scalar nodal values and the deformation matrix $\underline{\mathbf{B}}$, for vectorial nodal values, with the nodal values as well. The shape function matrix for scalar valued nodal values:

$$N = \begin{pmatrix} N_1 & \dots & N_k & \dots & N_n \end{pmatrix}. \tag{B.1}$$

Shape function matrix for vector valued nodal values:

$$\underline{\mathbf{N}} = \begin{pmatrix} N_1 & 0 & 0 & \dots & N_k & 0 & 0 & \dots & N_n & 0 & 0 \\ 0 & N_1 & 0 & \dots & 0 & N_k & 0 & \dots & 0 & N_n & 0 \\ 0 & 0 & N_1 & \dots & 0 & 0 & N_k & \dots & 0 & 0 & N_n \end{pmatrix}. \tag{B.2}$$

Gradient operator for the gradient of scalar valued nodal values:

$$B = \begin{pmatrix} N_{1,x} & \dots & N_{k,x} & \dots & N_{n,x} \\ N_{1,y} & \dots & N_{k,y} & \dots & N_{n,y} \\ N_{1,z} & \dots & N_{k,z} & \dots & N_{n,z} \end{pmatrix}, \tag{B.3}$$

Gradient operator for the gradient of vector valued nodal values:

$$\underline{\mathbf{B}} = \begin{pmatrix} N_{1,x} & 0 & 0 & \dots & N_{k,x} & 0 & 0 & \dots & N_{n,x} & 0 & 0 \\ 0 & N_{1,y} & 0 & \dots & 0 & N_{k,y} & 0 & \dots & 0 & N_{n,y} & 0 \\ 0 & 0 & N_{1,z} & \dots & 0 & 0 & N_{k,z} & \dots & 0 & 0 & N_{n,z} \\ N_{1,y} & N_{1,x} & 0 & \dots & N_{k,y} & N_{k,x} & 0 & \dots & N_{n,y} & N_{n,x} & 0 \\ N_{1,z} & 0 & N_{1,x} & \dots & N_{k,z} & 0 & N_{k,x} & \dots & N_{n,z} & 0 & N_{n,x} \\ 0 & N_{1,z} & N_{1,y} & \dots & 0 & N_{k,z} & N_{k,y} & \dots & 0 & N_{n,z} & N_{n,y} \end{pmatrix}. \tag{B.4}$$

The above gradient operator allow to calculate the symmetric gradient under the form of the Mandel tensor:

$$\underset{\sim}{\boldsymbol{\varepsilon}} = \begin{pmatrix} \varepsilon_{xx} \\ \varepsilon_{yy} \\ \varepsilon_{zz} \\ \sqrt{2}\,\varepsilon_{xy} \\ \sqrt{2}\,\varepsilon_{xz} \\ \sqrt{2}\,\varepsilon_{yz} \end{pmatrix}. \tag{B.5}$$

The stress can then be computed after separating the elastic part of the total strain with the elasticity tensor $\underline{\underline{\boldsymbol{\Lambda}}}$, that can be here reduced into a 6×6 matrix:

$$\underset{\sim}{\boldsymbol{\sigma}} = \underline{\underline{\boldsymbol{\Lambda}}} : \underset{\sim}{\boldsymbol{\varepsilon}}_e. \tag{B.6}$$

Balance equations (9) are then evaluated at each element from a Gauss integration procedure:

$$\begin{aligned} &\sum_q \left(\pi(q) N(q)\{u^*\} - [\underline{\boldsymbol{\xi}}](q) \cdot \mathbf{B}(q)\{u^*\}\right) W(q) = \sum_r \zeta(r) N(r)\{u^*\} W(r), \\ &\sum_q \left(\dot{c}_i(q) N(q)\{v^*\} - [\underline{\boldsymbol{J}}_i](q) \cdot \mathbf{B}(q)\{v^*\}\right) W(q) = \sum_r j_i(r) N(r)\{v^*\} W(r), \\ &\sum_q [\underline{\boldsymbol{\sigma}}](q) \cdot \underline{\mathbf{B}}(q)\{\underline{\boldsymbol{w}}^*\} W(q) = \sum_r [\underline{\boldsymbol{t}}](r) \cdot \mathbf{N}(r)\{\underline{\boldsymbol{w}}^*\} W(r). \end{aligned} \tag{B.7}$$

The residuals are then defined as follows:

$$\{R_\phi\} = \sum_q \left(N(q)\pi(q) - \mathbf{B}^T(q)[\underline{\boldsymbol{\xi}}](q)\right)W(q) - \sum_r N(r)\zeta(r)W(r),$$

$$\{R_{c_i}\} = \sum_q \left(N(q)\dot{c}_i(q) - \mathbf{B}^T(q)[\underline{\boldsymbol{J}}_i](q)\right)W(q) - \sum_r N(r)j_i(r)W(r),$$

$$\{R_{\underline{\boldsymbol{u}}}\} = \sum_q \underline{\mathbf{B}}^T(q)[\underline{\underline{\boldsymbol{\sigma}}}](q)W(q) - \sum_r \mathbf{N}^T(r)[\underline{\boldsymbol{t}}](r)\,W(r). \tag{B.8}$$

The multiphysical element has now the following ordering of the degrees of freedom:

$$\begin{pmatrix} \{\phi\} \\ \{c_i\} \\ \{\underline{\boldsymbol{u}}\} \end{pmatrix}, \tag{B.9}$$

which results in the following Jacobian:

$$J = \begin{pmatrix} \frac{\partial\{R_\phi\}}{\partial\{\phi\}} & \cdots & \frac{\partial\{R_\phi\}}{\partial\{c_i\}} & \cdots & \frac{\partial\{R_\phi\}}{\partial\{\underline{\boldsymbol{u}}\}} \\ \vdots & \ddots & \vdots & & \vdots \\ \frac{\partial\{R_{c_i}\}}{\partial\{\phi\}} & \cdots & \frac{\partial\{R_{c_i}\}}{\partial\{c_j\}} & \cdots & \frac{\partial\{R_{c_i}\}}{\partial\{\underline{\boldsymbol{u}}\}} \\ \vdots & & \vdots & \ddots & \vdots \\ \frac{\partial\{R_{\underline{\boldsymbol{u}}}\}}{\partial\{\phi\}} & \cdots & \frac{\partial\{R_{\underline{\boldsymbol{u}}}\}}{\partial\{c_i\}} & \cdots & \frac{\partial\{R_{\underline{\boldsymbol{u}}}\}}{\partial\{\underline{\boldsymbol{u}}\}} \end{pmatrix}, \tag{B.10}$$

used in the further calculation of the global stiffness matrix, which is not symmetric.

The sub-matrices of J read, regarding the phase field nodal value:

$$\begin{aligned} \frac{\partial\{R_\phi\}}{\partial\{\phi\}} &= \sum_q \left(N \otimes N(q)\frac{\partial\pi}{\partial\phi}(q) - \mathbf{B}^T(q)\frac{\partial[\underline{\boldsymbol{\xi}}]}{\partial\{\phi\}}(q)\right)W(q) \\ \frac{\partial\{R_\phi\}}{\partial\{c_i\}} &= \sum_q \left(N \otimes N(q)\frac{\partial\pi}{\partial c_i}(q) - \mathbf{B}^T(q)\frac{\partial[\underline{\boldsymbol{\xi}}]}{\partial\{c_i\}}(q)\right)W(q) \\ \frac{\partial\{R_\phi\}}{\partial\{\underline{\boldsymbol{u}}\}} &= \sum_q \left(N^T(q)\frac{\partial\pi}{\partial\{\underline{\boldsymbol{u}}\}}(q) - \mathbf{B}^T(q)\frac{\partial[\underline{\boldsymbol{\xi}}]}{\partial\{\underline{\boldsymbol{u}}\}}(q)\right)W(q), \end{aligned} \tag{B.11}$$

and, for concentrations:

$$\begin{aligned} \frac{\partial\{R_{c_i}\}}{\partial\{\phi\}} &= \sum_q \left(N \otimes N(q)\frac{\partial\dot{c}_i}{\partial\phi}(q) - \mathbf{B}^T(q)\frac{\partial[\underline{\boldsymbol{J}}_i]}{\partial\{\phi\}}(q)\right)W(q) \\ \frac{\partial\{R_{c_i}\}}{\partial\{c_j\}} &= \sum_q \left(N \otimes N(q)\frac{\partial\dot{c}_i}{\partial c_j}(q) - \mathbf{B}^T(q)\frac{\partial[\underline{\boldsymbol{J}}_i]}{\partial\{c_j\}}(q)\right)W(q) \\ \frac{\partial\{R_{c_i}\}}{\partial\{\underline{\boldsymbol{u}}\}} &= \sum_q \left(N^T(q)\frac{\partial\dot{c}_i}{\partial\{\underline{\boldsymbol{u}}\}}(q) - \mathbf{B}^T(q)\frac{\partial[\underline{\boldsymbol{J}}_i]}{\partial\{\underline{\boldsymbol{u}}\}}(q)\right)W(q), \end{aligned} \tag{B.12}$$

and lastly for displacements:

$$\begin{aligned} \frac{\partial\{R_{\underline{\boldsymbol{u}}}\}}{\partial\{\phi\}} &= \sum_q \underline{\mathbf{B}}^T(q)\frac{\partial[\underline{\underline{\boldsymbol{\sigma}}}]}{\partial\{\phi\}}(q)W(q) \\ \frac{\partial\{R_{\underline{\boldsymbol{u}}}\}}{\partial\{c_i\}} &= \sum_q \underline{\mathbf{B}}^T(q)\frac{\partial[\underline{\underline{\boldsymbol{\sigma}}}]}{\partial\{c_i\}}(q)W(q) \\ \frac{\partial\{R_{\underline{\boldsymbol{u}}}\}}{\partial\{\underline{\boldsymbol{u}}\}} &= \sum_q \underline{\mathbf{B}}^T(q)\frac{\partial[\underline{\underline{\boldsymbol{\sigma}}}]}{\partial\{\underline{\boldsymbol{u}}\}}(q)W(q). \end{aligned} \tag{B.13}$$

B.1. Derivatives for the Voigt/Taylor approach

In the Voigt/Taylor approach, π reads:

$$\pi = -\frac{1}{M_\pi}\dot{\phi} - Wg'(\phi) - h'(\phi)F_\phi, \tag{B.14}$$

where

$$F_\phi = f^\alpha - f^\beta - \mu_i\left(c_i^\alpha - c_i^\beta\right), \tag{B.15}$$

which leads to the following derivatives:

$$\begin{aligned}\frac{\partial\pi}{\partial\phi} &= -\frac{1}{M_\phi}\frac{\partial\dot{\phi}}{\partial\phi} - Wg''(\phi) - h''(\phi)F_\phi\\ \frac{\partial\pi}{\partial c_i} &= -h'k_i^\alpha\left(c_i^\alpha - c_i^\beta\right)\end{aligned} \tag{B.16}$$

and

$$\frac{\partial\pi}{\partial\{u\}} = \frac{\partial\pi}{\partial\underset{\sim}{\boldsymbol{\varepsilon}}}\frac{\partial\underset{\sim}{\boldsymbol{\varepsilon}}}{\partial\{\underline{\boldsymbol{u}}\}} = -h'\left(\frac{\partial f^\alpha}{\partial\underset{\sim}{\boldsymbol{\varepsilon}}} - \frac{\partial f^\beta}{\partial\underset{\sim}{\boldsymbol{\varepsilon}}}\right)\underline{\mathbf{B}} = -h'\left(\frac{\partial f^\alpha}{\partial\underset{\sim}{\boldsymbol{\varepsilon}}_e^\alpha}\frac{\partial\underset{\sim}{\boldsymbol{\varepsilon}}_e^\alpha}{\partial\underset{\sim}{\boldsymbol{\varepsilon}}} - \frac{\partial f^\beta}{\partial\underset{\sim}{\boldsymbol{\varepsilon}}_e^\beta}\frac{\partial\underset{\sim}{\boldsymbol{\varepsilon}}_e^\beta}{\partial\underset{\sim}{\boldsymbol{\varepsilon}}}\right)\underline{\mathbf{B}} = -h'\left(\underset{\sim}{\boldsymbol{\sigma}}^\alpha - \underset{\sim}{\boldsymbol{\sigma}}^\beta\right)\underline{\mathbf{B}} \tag{B.17}$$

Then using the state law (31) and (15), it comes:

$$\begin{aligned}\frac{\partial[\underline{\boldsymbol{\xi}}]}{\partial\{\phi\}} &= \frac{\partial[\underline{\boldsymbol{\xi}}]}{\partial\nabla\phi}\frac{\partial\nabla\phi}{\partial\{\phi\}} = 6\gamma\frac{\delta}{z}\underline{\mathbf{B}}\\ \frac{\partial[\underline{\boldsymbol{\xi}}]}{\partial\{c_i\}} &= 0\\ \frac{\partial[\underline{\boldsymbol{\xi}}]}{\partial\{\underline{\boldsymbol{u}}\}} &= 0\end{aligned} \tag{B.18}$$

The mass balance equation is rewritten taking the mixture rule (1) for c_i into account:

$$\begin{aligned}\frac{\partial\dot{c}_i}{\partial\phi} &= h'\left(1 - \frac{k_i^\alpha}{k_i^\beta}\right)\dot{c}_i^\alpha + \left(h''\dot{\phi} + h'\frac{\partial\dot{\phi}}{\partial\phi}\left(c_i^\alpha - c_i^\beta\right)\right)\\ \frac{\partial\dot{c}_i}{\partial c_i} &= h\frac{\partial\dot{c}_i^\alpha}{\partial c_i^\alpha} + \bar{h}\frac{\partial\dot{c}_i^\beta}{\partial c_i^\beta}\frac{k_i^\alpha}{k_i^\beta} + h'\dot{\phi}\left(1 - \frac{k_i^\alpha}{k_i^\beta}\right)\\ \frac{\partial\dot{c}_i}{\partial\{\underline{\boldsymbol{u}}\}} &= 0\end{aligned} \tag{B.19}$$

And for the flux (47), (48), (30) and (26):

$$\begin{aligned}\frac{\partial[\underline{\boldsymbol{J}}_i]}{\partial\{\phi\}} &= \frac{\partial[\underline{\boldsymbol{J}}_i]}{\partial\phi}\frac{\partial\phi}{\partial\{\phi\}} = -L_i'(\phi)\nabla\mu_i^\alpha N\\ \frac{\partial[\underline{\boldsymbol{J}}_i]}{\partial\{c_i\}} &= \frac{\partial[\underline{\boldsymbol{J}}_i]}{\partial\nabla c_i}\frac{\partial\nabla c_i}{\partial\{c_i\}} = -L_i(\phi)k_i^\alpha\underline{\mathbf{B}}\\ \frac{\partial[\underline{\boldsymbol{J}}_i]}{\partial\{\underline{\boldsymbol{u}}\}} &= 0\end{aligned} \tag{B.20}$$

Lastly, the Jacobian of the stress reads, recalling that $\underset{\sim}{\boldsymbol{\sigma}} = h\underset{\sim}{\boldsymbol{\sigma}}^\alpha + \bar{h}\underset{\sim}{\boldsymbol{\sigma}}^\beta$:

$$\begin{aligned}\frac{\partial\underset{\sim}{\boldsymbol{\sigma}}}{\partial\{\phi\}} &= \frac{\partial\underset{\sim}{\boldsymbol{\sigma}}}{\partial\phi}\frac{\partial\phi}{\partial\{\phi\}} = h'\left(\underset{\sim}{\boldsymbol{\sigma}}^\alpha - \underset{\sim}{\boldsymbol{\sigma}}^\beta\right)N\\ \frac{\partial\underset{\sim}{\boldsymbol{\sigma}}}{\partial\{c_i\}} &= 0\\ \frac{\partial\underset{\sim}{\boldsymbol{\sigma}}}{\partial\{\underline{\boldsymbol{u}}\}} &= \frac{\partial\underset{\sim}{\boldsymbol{\sigma}}}{\partial\underset{\sim}{\boldsymbol{\varepsilon}}}\frac{\partial\underset{\sim}{\boldsymbol{\varepsilon}}}{\partial\{\underline{\boldsymbol{u}}\}} = \left(h\underset{\approx}{\boldsymbol{\Lambda}}^\alpha + \bar{h}\underset{\approx}{\boldsymbol{\Lambda}}^\beta\right)\underline{\mathbf{B}} = \underset{\approx}{\boldsymbol{\Lambda}}^{\mathrm{eff}}\underline{\mathbf{B}}\end{aligned} \tag{B.21}$$

B.2. Derivatives for the Reuss/Sachs approach

The Reuss/Sachs approach differs from the Voigt/Taylor approach for two thermodynamic forces π and $\underset{\sim}{\boldsymbol{\sigma}}$. First π reads:

$$\pi = -\frac{1}{M_\pi}\dot{\phi} - Wg'(\phi) - h'(\phi)F_\phi, \tag{B.22}$$

where

$$F_\phi = f^\alpha - f^\beta - \sum_i \mu_i\left(c_i^\alpha - c_i^\beta\right) - \underset{\sim}{\boldsymbol{\sigma}}\colon\left(\underset{\sim}{\boldsymbol{\varepsilon}}^\alpha - \underset{\sim}{\boldsymbol{\varepsilon}}^\beta\right), \tag{B.23}$$

Moreover, the stresses are homogeneous, which reads:

$$\underset{\sim}{\boldsymbol{\sigma}} = \underset{\sim}{\boldsymbol{\sigma}}^\alpha = \underset{\sim}{\boldsymbol{\sigma}}^\beta \tag{B.24}$$

which leads to the following derivatives:

$$\begin{aligned}\frac{\partial\pi}{\partial\phi} &= -\frac{1}{M_\phi}\frac{\partial\dot{\phi}}{\partial\phi} - Wg''(\phi) - h''(\phi)F_\phi\\ \frac{\partial\pi}{\partial c_i} &= -h'k_i^\alpha\left(c_i^\alpha - c_i^\beta\right)\end{aligned} \tag{B.25}$$

and

$$\begin{aligned}\frac{\partial\pi}{\partial\{\underline{\boldsymbol{u}}\}} &= \frac{\partial\pi}{\partial\underset{\sim}{\boldsymbol{\sigma}}}\frac{\partial\underset{\sim}{\boldsymbol{\sigma}}}{\partial\{\underline{\boldsymbol{u}}\}} = -h'\frac{\partial}{\partial\underset{\sim}{\boldsymbol{\sigma}}}\left(-\frac{1}{2}\underset{\sim}{\boldsymbol{\sigma}}\colon S^\alpha\colon\underset{\sim}{\boldsymbol{\sigma}} + \frac{1}{2}\underset{\sim}{\boldsymbol{\sigma}}\colon S^\beta\colon\underset{\sim}{\boldsymbol{\sigma}} - \underset{\sim}{\boldsymbol{\sigma}}\colon\left(\underset{\sim}{\boldsymbol{\varepsilon}}_\star^{\,\alpha} - \underset{\sim}{\boldsymbol{\varepsilon}}_\star^{\,\beta}\right)\right)\underline{\mathbf{B}}\\ &= h'\frac{\partial}{\partial\underset{\sim}{\boldsymbol{\sigma}}}\left(\underset{\sim}{\boldsymbol{\sigma}}\colon\left(\frac{1}{2}\left(S^\alpha - S^\beta\right)\colon\underset{\sim}{\boldsymbol{\sigma}} + \underset{\sim}{\boldsymbol{\varepsilon}}_\star^{\,\alpha} - \underset{\sim}{\boldsymbol{\varepsilon}}_\star^{\,\beta}\right)\right)\underline{\mathbf{B}} = h'\left(\frac{1}{2}\left(\left(S^\alpha - S^\beta\right)\colon\underset{\sim}{\boldsymbol{\sigma}} + \underset{\sim}{\boldsymbol{\sigma}}\colon\left(S^\alpha - S^\beta\right)\right) + \underset{\sim}{\boldsymbol{\varepsilon}}_\star^{\,\alpha} - \underset{\sim}{\boldsymbol{\varepsilon}}_\star^{\,\beta}\right)\underset{\approx}{\boldsymbol{S}}^{\mathrm{eff}-1}\underline{\mathbf{B}}\end{aligned} \tag{B.26}$$

Finally, the Jacobian of the stress reads:

$$\begin{aligned}\frac{\partial\underset{\sim}{\boldsymbol{\sigma}}}{\partial\{\phi\}} &= \frac{\partial\underset{\sim}{\boldsymbol{\sigma}}}{\partial\phi}\frac{\partial\phi}{\partial\{\phi\}} = 0\\ \frac{\partial\underset{\sim}{\boldsymbol{\sigma}}}{\partial\{c_i\}} &= \frac{\partial\underset{\sim}{\boldsymbol{\sigma}}}{\partial c_i}\frac{\partial c_i}{\partial\{c_i\}} = 0\\ \frac{\partial\underset{\sim}{\boldsymbol{\sigma}}}{\partial\{\underline{\boldsymbol{u}}\}} &= \frac{\partial\underset{\sim}{\boldsymbol{\sigma}}}{\partial\underset{\sim}{\boldsymbol{\varepsilon}}}\frac{\partial\underset{\sim}{\boldsymbol{\varepsilon}}}{\partial\{\underline{\boldsymbol{u}}\}} = \left(h\underset{\approx}{\boldsymbol{S}}^\alpha + \bar{h}\underset{\approx}{\boldsymbol{S}}^\beta\right)^{-1}\underline{\mathbf{B}} = \underset{\approx}{\boldsymbol{S}}^{\mathrm{eff}-1}\underline{\mathbf{B}}\end{aligned} \tag{B.27}$$

References

Abrivard, G., Busso, E.P., Forest, S., Appolaire, B., 2012a. Phase field modeling of grain boundary motion driven by curvature and stored energy gradients. Part I: theory and numerical implementation. Philos. Mag. 92, 3618–3642.

Abrivard, G., Busso, E.P., Forest, S., Appolaire, B., 2012b. Phase field modeling of grain boundary motion driven by curvature and stored energy gradients. Part II: application to recrystallisation. Philos. Mag. 92, 3643–3664.

Ambati, M., Gerasimov, T., De Lorenzis, L., 2015. Phase-field modeling of ductile fracture. Comput. Mech. 55, 1017–1040.

Ammar, K., Appolaire, B., Cailletaud, G., Feyel, F., Forest, S., 2009a. Finite element formulation of a phase field model based on the concept of generalized stresses. Comput. Mat. Sci. 45, 800–805.

Ammar, K., Appolaire, B., Cailletaud, G., Forest, S., 2009b. Combining phase field approach and homogenization methods for modeling phase transformation in elastoplastic media. Eur. J. Comput. Mech. 18, 485–523.

Ammar, K., Appolaire, B., Cailletaud, G., Forest, S., 2011. Phase field modeling of elasto-plastic deformation induced by diffusion controlled growth of a misfitting spherical precipitate. Philos. Mag. Lett. 91, 164–172.

Ammar, K., Appolaire, B., Forest, S., Cottura, M., Le Bouar, Y., Finel, A., 2014. Modelling inheritance of plastic deformation during migration of phase boundaries using a phase field method. Meccanica 49, 2699–2717.

Appolaire, B., Le Bouar, Y., 2015. Second Order Asymptotics of a Phase Field with Elasticity, In Preparation.

Appolaire, B., Héricher, L., Aeby-Gautier, E., 2005. Modelling of phase transformation kinetics in Ti alloys—isothermal treatments. Acta Mater. 53, 3001–3011.

Appolaire, B., Aeby-Gautier, E., Dehmas, M., Denis, S., 2010. Non-coherent interfaces in diffuse interface models. Philos. Mag. 90, 461–483.

Asaro, R.J., Lubarda, V.A., 2006. Mechanics of Solids and Materials. University Press, Cambridge, UK.

Aslan, O., Forest, S., 2009. Crack growth modeling in single crystals based on higher order continua. Comput. Mater. Sci. 45, 756–761.

Aslan, O., Quilici, S., Forest, S., 2011a. Numerical modeling of fatigue crack growth in single crystals based on microdamage theory. Int. J. Damage Mech. 20, 681–705.

Aslan, O., Cordero, N.M., Gaubert, A., Forest, S., 2011b. Micromorphic approach to single crystal plasticity and damage. Int. J. Eng. Sci. 49, 1311–1325.

Aslan, O., Forest, S., 2011. The micromorphic versus phase field approach to gradient plasticity and damage with application to cracking in metal single crystals. In: de Borst, R., Ramm, E. (Eds.), Multiscale Methods in Computational Mechanics, pp. 135–154.

Besson, J., 2004. Local Approach to Fracture. École des Mines de Paris-Les Presses.

Besson, J., Cailletaud, G., Chaboche, J.-L., Forest, S., Blétry, M., 2009. Non-Linear Mechanics of Materials, Solid Mechanics and Its Applications, vol. 167. Springer, Paris.

Borden, M., Verhoosel, C., Scott, M., Hughes, T., Landis, C., 2012. A phase-field description of dynamic brittle fracture. Comput. Methods Appl. Mech. Eng. 217–220, 77–95.

Bösch, A., Müller-Krumbhaar, H., Shochet, O., 1995. Phase-field models for moving boundary problems: controlling metastability and anisotropy. Z. Phys. 97, 367–377.

Busso, E.P., Cailletaud, G., 2005. On the selection of active slip systems in crystal plasticity. Int. J. Plast. 21, 2212–2231.

Cahn, J.W., Hilliard, J.E., 1958. Free energy of a nonuniform system. I. Interfacial free energy. J. Chem. Phys. 28, 258–267.

Cahn, J.W., Larché, F., 1984. A simple model for coherent equilibrium. Acta Metall. 11, 1915–1923.
Coleman, B.D., Noll, W., 1963. The thermodynamics of elastic materials with heat conduction and viscosity. Arch. Ration. Mech. Anal. 13, 167–178.
Cottura, M., Le Bouar, Y., Finel, A., Appolaire, B., Ammar, K., Forest, S., 2012. A phase field model incorporating strain gradient viscoplasticity: application to rafting in Ni-base superalloys. J. Mech. Phys. Solids 60, 1243–1256.
Cottura, M., Appolaire, B., Finel, A., LeBouar, Y., 2015. Plastic relaxation during growth of Widmanstätten plates. Scripta Mater. 108, 117–121.
de Groot, S.R., Mazur, P., 1962. Non-equilibrium Thermodynamics. North-Holland, Dover.
de Rancourt, V., 2015. Modelling the Oxidation of Polycrystalline Austenitic Stainless Steels Using a Phase Field Approach Coupled with Mechanics (Ph.D. thesis). École des Mines ParisTech.
Dreyer, W., Müller, W.H., 2000. A study of the coarsening in tin/lead solders. J. Solids Struct. 37, 3841–3871.
Durga, A., Wollants, P., Moelans, N., 2013. Evaluation of interfacial excess contributions in different phase-field models for elastically inhomogeneous systems. Mod. Sim. Mater. Sci. Eng. 21, 055018.
Embury, J.D., Deschamps, A., Bréchet, Y., 2003. The interaction of plasticity and diffusion controlled precipitation reactions. Scr. Mater. 49, 927–932.
Finel, A., Le Bouar, Y., Gaubert, A., Salman, U., 2010. Phase field methods: microstructures, mechanical properties and complexity. C. R. Phys. 11, 245–256.
Forest, S., 2009. The micromorphic approach for gradient elasticity, viscoplasticity and damage. ASCE J. Eng. Mech. 135, 117–131.
Forest, S., Ammar, K., Appolaire, B., 2011. Micromorphic vs. phase–field approaches for gradient viscoplasticity and phase transformations. In: Markert, B. (Ed.), Advances in Extended and Multifield Theories for Continua, pp. 69–88.
Forest, S., Ammar, K., Appolaire, B., Cordero, N.M., Gaubert, A., 2014. Micromorphic approach to crystal plasticity and phase transformation. In: Schroeder, J., Hackl, K. (Eds.), Plasticity and beyond. CISM International Centre for Mechanical Sciences, Courses and Lectures, vol. 550. Springer, Vienna, pp. 131–198.
François, D., Pineau, A., Zaoui, A., 2012. Mechanical behaviour of materials. In: Micro and Macroscopic Constitutive Behaviour, Solid Mechanics and its Applications, vol. 180. Springer, Heidelberg.
Frolov, T., Mishin, Y., 2012. Thermodynamics of coherent interfaces under mechanical stresses. I. Theory. Phys. Rev. B 85, 224106.
Gaubert, A., Finel, A., Le Bouar, Y., Boussinot, G., 2008. Viscoplastic phase field modeling of rafting in Ni base superalloys. In: Jeulin, D., Forest, S. (Eds.), Continuum Models and Discrete Systems CMDS11. Mines Paris Les Presses, Paris, pp. 161–166.
Gaubert, A., Le Bouar, Y., Finel, A., 2010. Coupling phase field and viscoplasticity to study rafting in Ni-based superalloys. Philos. Mag. 90, 375–404.
Germain, P., Nguyen, Q.S., Suquet, P., 1983. Continuum thermodynamics. J. Appl. Mech. 50, 1010–1020.
Geslin, P.A., Appolaire, B., Finel, A., 2014. Investigation of coherency loss by prismatic punching with a nonlinear elastic model. Acta Mater. 71, 80–88.
Guo, X.H., Shi, S.Q., Ma, X.Q., 2005. Elastoplastic phase field model for microstructure evolution. Appl. Phys. Lett. 87, 221910.
Gurtin, M.E., 1996. Generalized Ginzburg–Landau and Cahn–Hilliard equations based on a microforce balance. Physica D 92, 178–192.
Halphen, B., Nguyen, Q.S., 1975. Sur les matériaux standard généralisés. J. Méc. 14, 39–63.
Hillert, M., 1999. Solute drag, solute trapping and diffusional dissipation of Gibbs energy. Acta Mater. 47, 4481–4905.
Hofacker, M., Miehe, C., 2012. Continuum phase field modeling of dynamic fracture: variational principles and staggered FE implementation. Int. J. Fract. 178, 113–129.
Hofacker, M., Miehe, C., 2013. A phase field model of dynamic fracture: robust field updates for the analysis of complex crack patterns. Int. J. Numer. Methods Eng. 93, 276–301.
Husain, S.W., Ahmed, M.S., Qamar, I., 1999. Dendritic morphology observed in the solid-state precipitation in binary alloys. Metal. Mater. Trans. A 30, 1529–1534.
Johnson, W.C., Alexander, J.I.D., 1986. Interface conditions for thermomechanical equilibrium in two-phase crystals. J. Appl. Phys. 59, 2735–2746.
Johnson, W.C., 1987. On the inapplicability of Gibbs phase rule to coherent solids. Metal. Trans. A 18, 1093–1097.
Johnson, W.C., Voorhees, P.W., 1999. Interfacial stress, interfacial energy, and phase equilibria in binary alloys. J. Stat. Phys. 95, 1281–1309.
Karma, A., Rappel, W.J., 1998. Quantitative phase-field modeling of dendritic growth in two and three dimensions. Phys. Rev. E 57, 4323–4349.
Kim, S.G., Kim, W.T., Suzuki, T., 1999. Phase-field model for binary alloys. Phys. Rev. E 60, 7186–7197.
Lemaitre, J., Chaboche, J.-L., 1994. Mechanics of Solid Materials. Cambridge University Press, Cambridge.
Lemaitre, J., Desmorat, R., 2004. Engineering damage mechanics: ductile, creep, fatigue and brittle failures. Springer-Verlag, Berlin.
Leo, P.H., Sekerka, R.F, 1989. The effect of elastic fields on the morphological stability of a precipitate grown from solid solution. Acta Metal 37, 3139–3149.
Maugin, G.A., 1992. Thermomechanics of plasticity and fracture. Cambridge University Press, Cambridge.
Maugin, G.A., 1999. Thermomechanics of Nonlinear Irreversible Behaviors. World Scientific, Singapore.
Miehe, C., Welchinger, F., Hofacker, M., 2010. Thermodynamically-consistent phase field models of fracture: variational principles and multifield FE implementations. Int. J. Numer. Methods Eng. 83, 1273–1311.
Mosler, J., Shchyglo, O., Montazer, H., 2014. A novel homogenization method for phase field approaches based on partial rank-one relaxation. J. Mech. Phys. Solids 68, 251–266.
Müller, I., 2001. Thermodynamics of mixtures and phase field theory. Int. J. Solids Struct. 38, 1105–1113.
Mullins, W.W., Sekerka, R.F., 1963. Morphological stability of a particle growing by diffusion or heat flow. J. Appl. Phys. 34, 323–329.
Perevoshchikova, N., 2012. Modeling of Austenite to Ferrite Transformation in Steels (Ph.D. thesis). Université de Lorraine.
Perevoshchikova, N., Appolaire, B., Teixeira, J., Aeby-Gautier, E., Denis, S., 2014. Investigation of the growth kinetics of $\gamma \rightarrow \alpha$ in Fe–C–X alloys with a thick interface model. Comput. Mater. Sci. 82, 151–158.
Plapp, M., 2011. Unified derivation of phase-field models for alloy solidification from a grand-potential functional. Phys. Rev. E 84, 031601.
Qu, J., Cherkaoui, M., 2006. Fundamentals of Micromechanics of Solids. John Wiley & Sons Inc, Hoboken.
Sanchez-Palencia, E., Zaoui, A., 1987. Homogenization techniques for composite media. In: Lecture Notes in Physics, vol. 272, Springer, Berlin.
Schmitt, R., Kuhn, C., Müller, R., Bhattacharya, K., 2014. Crystal plasticity and martensitic transformations—a phase field approach. Techn. Mech. 34, 23–38.
Spatschek, R., Eidel, B., 2013. Driving forces for interface kinetics and phase field models. Int. J. Sol. Struct. 50, 2424–2436.
Steinbach, I., Apel, M., 2006. Multi phase field model for solid state transformation with elastic strain. Physica D 217, 153–160.
Steinbach, I., 2009. Phase-field models in materials science. Model. Simul. Mater. Sci. Eng. 17, 073001.
Tiaden, J., Nestler, B., Diepers, H.J., Steinbach, I., 1998. The multiphase-field model with an integrated concept for modeling solute diffusion. Physica D 115, 73–86.
Ubachs, R.L.J.M., Schreurs, P.J.G., Geers, M.G.D., 2005. Phase field dependent viscoplastic behavior of solder alloys. Int. J. Sol. Struct. 42, 2533–2558.
Uehara, T., Tsujino, T., Ohno, N., 2007. Elasto-plastic simulation of stress evolution during grain growth using a phase field model. J. Cryst. Growth 300, 530–537.
Vignollet, J., May, S., de Borst, R., Verhoosel, C.V., 2014. Phase-field models for brittle and cohesive fracture. Meccanica 49, 2587–2601.
Villani, A., Busso, E.P., Ammar, K., Forest, S., Geers, M.G.D., 2014. A fully coupled diffusional-mechanical formulation: numerical implementation, analytical validation, and effects of plasticity on equilibrium. Arch. Appl. Mech. 84, 1647–1664.
Voyiadjis, G.Z., Mozaffari, N., 2013. Nonlocal damage model using the phase field method: theory and applications. Int. J. Solids Struct. 50, 3136–3151.
Wang, Y., Khachaturyan, A.G., Morris Jr., J.W., 1993. Kinetics of strain-induced morphological transformation in cubic alloys with a miscibility gap. Acta Metall. Mater. 41, 279–296.
Wang, S.L., Sekerka, R.F., Wheeler, A.A., Murray, B.T., Coriell, S.R., Braun, R.J., McFadden, G.B., 1993. Thermodynamically-consistent phase-field models for solidification. Physica D 69, 189–200.
Yamanaka, A., Takaki, T., Tomita, Y., 2008. Elastoplastic phase-field simulation of self- and plastic accommodations in Cubic → tetragonal martensitic transformation. Mater. Sci. Eng. A 491, 378–384.
Zaoui, A., 2002. Continuum micromechanics: survey. ASCE J. Eng. Mech. 128, 808–816.